

1 **Simulation of atmospheric N₂O with GEOS-Chem and its** 2 **adjoint: evaluation of observational constraints**

3

4 **K. C. Wells¹, D. B. Millet¹, N. Boussez², D. K. Henze², S. Chaliyakunnel¹, T. J.**
5 **Griffis¹, Y. Luan¹, E. J. Dlugokencky³, R. G. Prinn⁴, S. O'Doherty⁵, R. F. Weiss⁶,**
6 **G. S. Dutton^{3,7}, J. W. Elkins³, P. B. Krummel⁸, R. Langenfelds⁸, L. P. Steele⁸, E.**
7 **A. Kort⁹, S. C. Wofsy¹⁰, T. Umezawa^{11,12}**

8 [1] {Department of Soil, Water, and Climate, University of Minnesota, St. Paul, Minnesota,
9 USA}

10 [2] {Department of Mechanical Engineering, University of Colorado at Boulder, Boulder,
11 Colorado, USA}

12 [3] {Earth System Research Laboratory, NOAA, Boulder, Colorado, USA}

13 [4] {Center for Global Change Science, Massachusetts Institute of Technology, Cambridge,
14 Massachusetts, USA}

15 [5] {School of Chemistry, University of Bristol, Bristol, UK}

16 [6] {Scripps Institute of Oceanography, University of California, San Diego, La Jolla,
17 California, USA}

18 [7] {CIRES, University of Colorado, Boulder, Colorado, USA}

19 [8] {CSIRO Oceans and Atmosphere Flagship, Aspendale, Victoria, Australia}

20 [9] {Department of Atmospheric, Oceanic, and Space Sciences, University of Michigan, Ann
21 Arbor, Michigan, USA}

22 [10] {School of Engineering and Applied Science and Department of Earth and Planetary
23 Sciences, Harvard University, Cambridge, Massachusetts, USA}

24 [11] {Center for Atmospheric and Oceanic Studies, Tohoku University, Sendai, Japan}

25 [12] {Max-Planck Institute for Chemistry, Mainz, Germany}

26 Correspondence to: D. B. Millet (dbm@umn.edu)

1
2
3
4
5
6
7
8
9
10
11
12
13
14
15
16
17
18
19
20
21
22
23
24
25
26
27
28
29
30
31

Abstract

We describe a new 4D-Var inversion framework for N₂O based on the GEOS-Chem chemical transport model and its adjoint, and apply it in a series of observing system simulation experiments to assess how well N₂O sources and sinks can be constrained by the current global observing network. The employed measurement ensemble includes approximately weekly and quasi-continuous N₂O measurements (hourly averages used) from several long-term monitoring networks, N₂O measurements collected from discrete air samples onboard a commercial aircraft (CARIBIC), and quasi-continuous measurements from an airborne pole-to-pole sampling campaign (HIPPO). For a two-year inversion, we find that the surface and HIPPO observations can accurately resolve a uniform bias in emissions during the first year; CARIBIC data provide a somewhat weaker constraint. Variable emission errors are much more difficult to resolve given the long lifetime of N₂O, and major parts of the world lack significant constraints on the seasonal cycle of fluxes. Current observations can largely correct a global bias in the stratospheric sink of N₂O if emissions are known, but do not provide information on the temporal and spatial distribution of the sink. However, for the more realistic scenario where source and sink are both uncertain, we find that simultaneously optimizing both would require unrealistically small errors in model transport. Regardless, a bias in the magnitude of the N₂O sink would not affect the a posteriori N₂O emissions for the two-year timescale used here, given realistic initial conditions, due to the timescale required for stratosphere-troposphere exchange (STE). The same does not apply to model errors in the rate of STE itself, which we show exerts a larger influence on the tropospheric burden of N₂O than does the chemical loss rate over short (< 3 year) timescales. We use a stochastic estimate of the inverse Hessian for the inversion to evaluate the spatial resolution of emission constraints provided by the observations, and find that significant, spatially explicit constraints can be achieved in locations near and immediately upwind of surface measurements and the HIPPO flight tracks; however, these are mostly confined to North America, Europe, and Australia. None of the current observing networks are able to provide significant spatial information on tropical N₂O emissions. There, averaging kernels (describing the sensitivity of the inversion to emissions in each grid square) are highly smeared spatially and extend even to the midlatitudes, so that tropical emissions risk being

1 conflated with those elsewhere. For global inversions, therefore, the current lack of constraints
2 on the tropics also places an important limit on our ability to understand extratropical
3 emissions. Based on the error reduction statistics from the inverse Hessian, we characterize
4 the atmospheric distribution of unconstrained N₂O, and identify regions in and downwind of
5 South America, Central Africa, and Southeast Asia where new surface or profile
6 measurements would have the most value for reducing present uncertainty in the global N₂O
7 budget.

8

9 **1 Introduction**

10 Nitrous oxide (N₂O) is a long-lived greenhouse gas with a global warming potential
11 approximately 300 times that of CO₂ on a 100-year timescale (Forster et al., 2007). It is also a
12 key player in stratospheric chemistry; N₂O emissions weighted by their ozone depletion
13 potential currently outrank those of any other ozone depleting substance (Ravishankara et al.,
14 2009). N₂O is produced via microbial nitrification and denitrification in soils (Firestone and
15 Davidson, 1989) and ocean waters (Elkins et al., 1978; Cohen and Gordon, 1979; Law and
16 Owens, 1990), with soils contributing the majority of the global flux (Mosier et al., 1998).
17 Agricultural activities such as fertilizer application and animal waste management increase the
18 substrate available for nitrification and denitrification pathways (Maggiotto et al., 2000),
19 leading to enhanced direct on-site emissions as well as indirect emissions downstream due to
20 leaching and runoff (IPCC, 2006). Energy production and transportation (Denman et al.,
21 2007) and biomass burning emissions (van der Werf et al., 2010) also contribute to the global
22 N₂O source. N₂O is lost in the stratosphere via photolysis and reaction with O(¹D), leading to
23 a global lifetime currently estimated at ~122-131 years (Volk et al., 1997; Prather et al.,
24 2012). Atmospheric N₂O is currently increasing at ~0.8 ppb yr⁻¹
25 (<http://ds.data.jma.go.jp/gmd/wdcgg/pub/global/globalmean.html>), driven by accelerating
26 human perturbation of the nitrogen cycle: in particular, rising application of nitrogen
27 fertilizers (Galloway et al., 2008; Davidson, 2009; Park et al., 2012) and the nonlinear
28 response of soil N₂O emissions to N inputs in excess of crop demands (Shcherbak et al.,
29 2014).

30 Rates of microbial nitrification and denitrification in soils depend strongly on environmental
31 characteristics such as temperature (Potter et al., 1996), moisture (Bouwman, 1998; Bouwman

1 et al., 2013), availability of reactive nitrogen substrate, and the make-up of the soil microbial
2 community (Butterbach-Bahl et al., 2013), and as a result large uncertainties exist in the
3 spatial and temporal distribution of global N₂O emissions. Long-term flask-based and in-situ
4 observations of atmospheric N₂O are available from a number of monitoring networks around
5 the world, along with routine and intensive aircraft observations, and there have been several
6 recent studies employing these data to generate top-down estimates of global N₂O emissions.
7 Huang et al. (2008) derived a global N₂O flux of 14.1-17.1 Tg N yr⁻¹ for 2002-2005 using
8 surface observations from four different surface monitoring networks. Based on aircraft
9 observations from the first two HIAPER Pole-to-Pole Observations (HIPPO) campaigns, Kort
10 et al. (2011) found evidence for large and episodic tropical fluxes. Saikawa et al. (2014)
11 combined surface observations with aircraft- and ship-based measurements to derive regional
12 N₂O emission estimates for five source sectors, and inferred a global flux of 18.1 ± 0.6 Tg N
13 yr⁻¹ for 2002-2005. Thompson et al. (2014a) used ground- and ship-based observations to
14 estimate regional N₂O emissions and their interannual variability. Their study yielded global
15 fluxes for 1999-2009 that ranged from 17.5 to 20.1 Tg N yr⁻¹, with interannual variability
16 driven largely by fluctuations in tropical and subtropical soil fluxes. A recent intercomparison
17 of top-down inversion results using different transport models gave a comparable range of
18 global fluxes: 16.1-18.7 Tg N yr⁻¹ for 2006-2009 (Thompson et al., 2014c).

19 Some previous work has found that uncertainties in stratosphere-troposphere exchange (STE)
20 and the associated influx of N₂O-depleted air can give rise to significant uncertainties in N₂O
21 source inversions, depending on the time range and scale over which the emissions are
22 optimized (Nevison et al., 2005; Hirsch et al., 2006; Huang et al., 2008). On the other hand,
23 Thompson et al. (2011) found their a posteriori surface fluxes to be quite insensitive to biases
24 in the N₂O stratospheric loss rate during the first year of a multi-year simulation. They also
25 found that combining surface and aircraft observations could provide some constraint on the
26 magnitude of the stratospheric N₂O sink in a simultaneous source-sink inversion, without
27 increasing errors in the a posteriori N₂O emissions. However, biases in the model STE itself
28 did give rise to regional uncertainties of up to 25% in the optimized source.

29 The global observing network for atmospheric N₂O includes flask-based measurements and
30 quasi-continuous in-situ instruments, as well as both surface- and airborne sampling
31 platforms. However, a full quantification of the relative utility of these different datasets has

1 not yet been performed. Such information is needed in order to determine: *i*) the degree to
2 which current observations can be used to constrain N₂O emissions and stratospheric loss, and
3 the comparative value of different observing strategies for doing so; *ii*) the spatial and
4 temporal resolution at which N₂O sources and sinks can be constrained by these different
5 datasets; and *iii*) where additional measurements are most needed to advance present
6 understanding of the atmospheric N₂O budget.

7 In this paper, we introduce a new simulation and inversion framework for atmospheric N₂O
8 using the GEOS-Chem chemical transport model (CTM) and its adjoint. The adjoint-based
9 variational method is advantageous as it allows us to solve for N₂O fluxes at the spatial
10 resolution of the CTM and at any desired time step, thus minimizing any impact from
11 aggregation errors. Here, we apply the model in a simulation environment (i.e., in observing
12 system simulation experiments, or OSSEs) to quantify the N₂O source and sink constraints
13 provided by: *i*) flask and quasi-continuous surface observations from a number of long-term
14 monitoring networks; *ii*) routine flask observations from an instrument platform deployed
15 onboard a commercial aircraft (Civil Aircraft for the Regular Investigation of the atmosphere
16 Based on an Instrument Container; CARIBIC); and *iii*) in situ airborne observations made
17 during a series of intensive pole-to-pole field campaigns (HIAPER Pole-to-Pole Observations;
18 HIPPO). This is the first study to quantify the individual constraints provided by these
19 different observation ensembles. We determine the potential for model errors in the
20 stratospheric loss rate of N₂O to bias the inferred emission estimates, and assess how well
21 N₂O emissions and stratospheric loss can be simultaneously constrained by the above
22 observations. We evaluate the temporal and spatial resolution of emission constraints afforded
23 by the different N₂O observations, and explore the impact of uncertainties in the a priori error
24 estimates on the inferred fluxes. Finally, we apply the above information to identify regions
25 that are underconstrained by the current N₂O observing network, and the downwind locations
26 where new measurements would be most valuable for reducing current uncertainty in the N₂O
27 budget.

28

29 **2 N₂O simulation in the GEOS-Chem CTM**

30 In this work we implement an N₂O simulation in the GEOS-Chem (<http://www.geos-chem.org>) global 3-D model of atmospheric chemistry. Analyses presented here use
31

1 assimilated meteorological data from the NASA Goddard Earth Observing System (GEOS-5),
2 degraded to a horizontal resolution of 4° latitude \times 5° longitude and to a vertical grid
3 containing 47 levels from the surface to 0.01 hPa. Transport is calculated on a 30 minute time
4 step; a 60 minute time step is used for emissions and chemistry. Our simulation period runs
5 from April 2010 to April 2012.

6 A priori N_2O emissions are grouped into four categories: anthropogenic (including industrial
7 processes, transportation, residential/waste management, and agricultural activities), natural
8 soil fluxes, biomass burning, and oceanic exchange. Annual emissions for anthropogenic
9 activities are obtained from the Emission Database for Global Atmospheric Research
10 (EDGARv4.2, <http://edgar.jrc.ec.europa.eu>). Within this database there are 12 emission
11 sectors as defined by the IPCC (IPCC, 2006). These sectors are listed in Table 1, along with
12 the corresponding total emissions for 2008. The overall anthropogenic N_2O flux from
13 EDGARv4.2 is 6.9 Tg N yr^{-1} , with 2.4 Tg N yr^{-1} from industrial and residential sources and
14 4.5 Tg N yr^{-1} from direct and indirect agricultural emissions. Natural soil emissions of N_2O
15 are computed based on the EDGARv2 database, which provides an annual flux at $1^\circ \times 1^\circ$
16 resolution for the year 1990 totaling 3.2 Tg N yr^{-1} . Biomass burning emissions of N_2O are
17 prescribed monthly based on the Global Fire Emissions Database version 3 (GFEDv3, van der
18 Werf et al., 2010) and total 0.6 Tg N yr^{-1} for 2010-2011. Thermal and biogeochemical oceanic
19 fluxes of N_2O are calculated monthly at $4.5^\circ \times 3.75^\circ$ following Jin and Gruber (2003), leading
20 to a net annual global source of 3.5 Tg N yr^{-1} . Figure 1 maps the resulting annual flux from
21 soils, anthropogenic activities, biomass burning, and air-sea exchange, with a cumulative
22 annual global source of $14.2 \text{ Tg N yr}^{-1}$. We note that this is below the range of current top-
23 down flux estimates (~ 16 to 20 Tg N yr^{-1}) discussed previously.

24 Stratospheric destruction of N_2O by photolysis and reaction with $\text{O}(^1\text{D})$ is calculated using
25 archived monthly 3-D loss frequencies from Global Modeling Initiative (GMI) simulations
26 driven by Modern Era Retrospective-Analysis for Research and Applications (MERRA)
27 meteorological fields (MERRA is also based on GEOS-5). The resulting stratospheric loss
28 gives rise to a 127.5 year lifetime, which is in the range of current estimates (122-131 years,
29 Volk et al., 1997; Prather et al., 2012). This lifetime depends upon the initial mass distribution
30 assumed for N_2O , which we describe below.

1 Because of the long atmospheric lifetime of N₂O, generating realistic initial conditions is of
 2 critical importance for top-down analyses of its sources and sinks. Some previous studies have
 3 included initial conditions as part of the state vector for optimization, or prescribed N₂O mass
 4 fields from simulations that have reached a pseudo-steady state. We instead construct an
 5 initial 3-D N₂O field using global observations for March 2010 (Fig. 2), one month prior to
 6 the start of our optimization window. This timing is chosen to accommodate a brief model
 7 spin-up that smooths any artificial horizontal gradients prescribed in the initial conditions.
 8 Initial tropospheric concentrations are computed from NOAA Carbon Cycle and Greenhouse
 9 Gases (CCGG) flask observations (described below) averaged monthly and zonally at 4°
 10 resolution. These mixing ratios are then assumed uniform from the surface to the tropopause.
 11 Above 100 hPa, our initial conditions are based on monthly mean (March 2010) N₂O profiles
 12 measured by the Microwave Limb Sounder (MLS) onboard the EOS Aura satellite (Lambert
 13 et al., 2007) interpolated onto the GEOS-Chem horizontal and vertical grid. Where needed,
 14 we then perform a linear interpolation between the tropopause and 100 hPa.

15

16 **3 Inversion set-up and verification**

17 We use a 4D-Var inversion framework to solve for spatially resolved, monthly N₂O fluxes
 18 based on the atmospheric measurements described next (Section 4). Optimal fluxes are
 19 derived by minimizing the cost function, $J(\mathbf{p})$, which contains contributions from the error
 20 weighted model-measurement differences and a penalty term:

$$21 \quad J(\mathbf{p}) = \frac{1}{2} \sum_{\mathbf{c} \in \Omega} (\mathbf{c} - \mathbf{y})^T \mathbf{S}_y^{-1} (\mathbf{c} - \mathbf{y}) + \frac{1}{2} \gamma (\mathbf{p} - \mathbf{p}_a)^T \mathbf{S}_a^{-1} (\mathbf{p} - \mathbf{p}_a) \quad (1)$$

22 Here, \mathbf{p} is the vector of parameters to be optimized, \mathbf{p}_a is the initial (a priori) value of those
 23 parameters, \mathbf{y} is a set of observations, \mathbf{c} is a vector containing the model-simulated
 24 concentrations, \mathbf{S}_y and \mathbf{S}_a are the observational and a priori emissions error covariance
 25 matrices, respectively, Ω is the time and space domain of the observations, and γ is a
 26 regularization parameter (set here to 1.0).

27 In this study, \mathbf{p} contains monthly scaling factors for the terrestrial and oceanic emissions of
 28 N₂O and for stratospheric loss frequencies. The adjoint model calculates the gradient of the
 29 cost function with respect to this state vector, $\nabla_p J(\mathbf{p})$, and employs a quasi-Newton

1 minimization routine to iteratively minimize $J(\mathbf{p})$ (Zhu et al., 1994; Byrd et al., 1995). Scale
2 factors for emissions are optimized on the $4^\circ \times 5^\circ$ GEOS-Chem grid, while those for the
3 stratospheric loss frequencies are aggregated over the vertical extent of the stratosphere and
4 into eight latitude bands of 22.5° . For the two-year inversion, this results in a state vector with
5 79,488 elements for emissions and 192 elements for stratospheric loss. We use a lower bound
6 of zero in the optimization routine to avoid a solution containing negative scaling factors and
7 an upper bound of 10 that was found to improve optimization performance. Use of the lower
8 bound corresponds to an implicit assumption that the sign of the a priori N_2O flux in each
9 location is correct, while the upper bound assumes that the a priori emissions are not biased
10 low by more than a factor of 10. Such bounds are not problematic for the synthetic
11 experiments presented here, but would affect real inversions if those assumptions were
12 violated.

13 We assume 100% uncertainty in the a priori emissions (for any given grid square and month)
14 and in the stratospheric loss frequencies, and impose horizontal correlation length scales for
15 emissions of 500 km over land and 1000 km over ocean, following Thompson et al. (2011;
16 2014a). The observational error covariance matrix contains contributions from the
17 measurement uncertainty (typically 0.4 ppb, see next section for details) and from model
18 transport errors. We estimate the latter from the variance in modeled N_2O mixing ratios across
19 all grid boxes adjacent to that containing a given observation. This results in mean errors of
20 0.2 ppb at the surface and 2-8 ppb at aircraft cruising altitudes.

21 The adjoint modules for optimizing N_2O emissions and stratospheric loss were verified by
22 comparing adjoint and finite difference sensitivities calculated for each atmospheric column
23 with no horizontal transport. We find good agreement between adjoint and finite difference
24 sensitivities for both emissions and stratospheric loss scaling factors (Fig. S1), demonstrating
25 the accuracy of the N_2O adjoint code. Propagation of adjoint sensitivities through horizontal
26 transport in the GEOS-Chem adjoint has been verified previously (Henze et al., 2007). The
27 GEOS-Chem adjoint has been used for a wide range of research applications such as
28 constraining sources of aerosols (Henze et al., 2007; Henze et al., 2009; Kopacz et al., 2011;
29 Wang et al., 2012; Xu et al., 2013), CO (Kopacz et al., 2009; Kopacz et al., 2010), NH_3 (Zhu
30 et al., 2013), O_3 (Zhang et al., 2009; Parrington et al., 2012), and methanol (Wells et al.,

1 2014), and to assess the impact of different types of observations on CO source inversions
2 (Jiang et al., 2011; Jiang et al., 2013).

3

4 **4 Global observations of atmospheric N₂O**

5 Below, we apply GEOS-Chem and its adjoint to assess the N₂O source and sink constraints
6 provided by the current suite of global observations. We include in this assessment several
7 long-term surface monitoring networks and two aircraft platforms. A full list of the surface
8 observation sites can be found in Table 2, and their locations are mapped in Fig. 3. The
9 majority of the surface observations are from discrete air samples collected approximately
10 weekly in flasks at 77 sites in the NOAA CCGG program (Dlugokencky et al., 1994), which
11 are analyzed using a gas chromatograph with an electron capture detector and reported on the
12 NOAA 2006A calibration scale. We also use flask measurements from six sites in the
13 Commonwealth Scientific and Industrial Research Organisation (CSIRO) network (also on
14 the NOAA 2006A scale; Francey et al., 1996; Cooper et al., 1999), five sites in the
15 Environment Canada (EC) network (NOAA 2006 scale), and one National Institute of Water
16 and Atmospheric research (NIWA) site (NOAA 2006A scale). We assume a measurement
17 uncertainty of 0.4 ppb for all of the above flask measurements, based on recommendations
18 from the data providers. Hourly averages of quasi-continuous measurements are employed
19 from six sites in the NOAA Chromatograph for Atmospheric Trace Species (CATS) network,
20 six sites in the Advanced Global Atmospheric Gases Experiment (AGAGE) network (Prinn et
21 al., 2000), and the University of Minnesota tall tower Trace Gas Observatory (KCMP tall
22 tower) site (Griffis et al., 2013). Measurements from the AGAGE network are reported on the
23 SIO-98 scale, and have a reported uncertainty of 0.2% (0.6 ppb). Measurements at the KCMP
24 tall tower and those in the CATS network (both on the NOAA 2006A scale) have
25 uncertainties of about 1.0 and 0.3 ppb, respectively.

26 Extensive airborne measurements of N₂O are available from the CARIBIC observatory
27 (Brenninkmeijer et al., 2007). CARIBIC provides flask measurements from a commercial
28 Lufthansa aircraft, with data available for 79 flights between Frankfurt, Germany and a
29 number of other cities around the world (Fig. 3) during the time period of our optimization.
30 These observations have an uncertainty of about 0.35 ppb and are reported on the NOAA
31 2006 scale (Schuck et al., 2009). Since the CARIBIC observatory is operated on a passenger

1 aircraft, the majority of measurements are taken at a cruising altitude of 9-12 km: about 50%
2 are in the lowermost stratosphere (in general those at higher latitudes, depending on synoptic
3 conditions), with the remainder sampling the upper troposphere (Assonov et al., 2013;
4 Umezawa et al., 2014).

5 High-frequency airborne N₂O measurements were made by quantum cascade laser
6 spectroscopy (QCLS) during the HIPPO campaigns (Wofsy, 2011; flight tracks mapped in
7 Fig. 3). Three of the five HIPPO deployments took place during our optimization window:
8 HIPPO III (24 March – 16 April 2010), HIPPO IV (14 June – 11 July 2011), and HIPPO V (9
9 August – 9 September 2011), totaling 33 flights over the April 2010 – April 2012 time frame.
10 Measurements are reported on the NOAA 2006 scale (Kort et al., 2011). The HIPPO flights
11 range from pole-to-pole while profiling the atmosphere from the surface to the tropopause at
12 regular intervals. Unlike the other available datasets, which provide recurrent measurements at
13 discrete locations or along specific flight paths, the HIPPO datasets provide ~1-month global
14 cross-sections of atmospheric concentration.

15 The use of different calibration scales results in offsets between different networks measuring
16 N₂O, which may also vary with time. Because variability in atmospheric N₂O is low, these
17 offsets can have a significant impact on the a posteriori solution. As the results presented here
18 involve synthetic observations at the time and location of the real observations, we do not
19 consider the impact of these offsets on inferred N₂O emissions and stratospheric loss.
20 However, for inversions employing real N₂O measurements, we calculate offsets at collocated
21 sites to adjust those measurements that are not reported on the NOAA 2006A scale.

22

23 **5 Evaluating constraints on N₂O emissions and stratospheric loss using** 24 **pseudo observations**

25 In this section we perform a range of pseudo observation tests to determine how well N₂O
26 sources (and sinks) can be quantified, and at what space-time resolution, based on the
27 observing network described above. In these tests, we sample the model at the time and
28 location of each observation to generate pseudo observations. A subset of tests were carried
29 out with observational (measurement + transport) noise added to the synthetic observations,
30 and these yielded the same results as the tests with no noise. We then perform a two-year

1 inversion in which we assimilate pseudo observations generated for the surface network,
2 CARIBIC flights, or HIPPO flights. Our state vector contains monthly scaling factors for
3 emissions, stratospheric loss frequencies, or both. We start with a spatially-uniform incorrect a
4 priori value for these scaling factors; this bias is temporally uniform in most tests, though later
5 we also test the impact of a seasonally varying emission bias. The degree to which the
6 optimization converges to the true value of 1.0 for each grid cell and month gives a measure
7 of the ability of the observations to correct for model biases in these processes. Section 5.1
8 presents tests in which we optimize emissions using the three observational datasets, Section
9 5.2 contains tests in which we optimize stratospheric loss frequencies alone or jointly with
10 emissions, and Section 5.3 describes tests in which we optimize emissions with a seasonal a
11 priori bias imposed. A full list of all pseudo observation tests performed is given in Table 3.

12 **5.1 Constraints on N₂O emissions**

13 Figure 4 shows the results of synthetic inversions in which we optimize emissions using
14 surface-based pseudo observations as described above. Here we impose a time invariant a
15 priori emission bias of $\pm 50\%$ across all land and ocean grid cells, while keeping the
16 stratospheric loss rates fixed at their true model values. We see that for the first ~ 20 months of
17 the optimization window, the surface-based inversion is able to correct the imposed bias over
18 most land and ocean regions that have a significant flux. However we will show later that this
19 does not mean current observations can fully constrain the spatial distribution of N₂O
20 emissions at the $4^\circ \times 5^\circ$ resolution shown in Fig. 4.

21 Overall, the solution is of comparable quality whether we start with a high or low a priori bias,
22 with some minor distinctions: the test with the positive initial bias performs slightly better
23 over oceans and in later months of the simulation, and also converges more quickly (5
24 iterations versus 10 for the test with a low initial bias). However, the situation is very different
25 when no upper bound is imposed on the solution. In this case, when given a low initial bias
26 the optimization tends to overshoot the truth in high-flux regions while underestimating the
27 truth in low-flux regions. Imposing both lower and upper bounds on the inverse solution (in
28 this case, 0 and 10) is thus important to ensure a consistent solution across high and low initial
29 bias scenarios. Jiang et al. (2014) concluded that construction of the a priori constraint was the
30 most important factor affecting the consistency of solutions for divergent initial assumptions

1 in the case of CO; we find here that the prior bounds placed on the solution can have a
2 comparable impact for N₂O.

3 Figure 4 also indicates that during the last several months of the optimization window there is
4 inadequate forcing for the inversion to completely correct for the initial emission biases,
5 particularly over the Southern Hemisphere. This is largely due to the timescale required to
6 transport N₂O between source regions and receptor locations—in the Southern Hemisphere
7 observing stations are sparse and distant from major N₂O sources. As a result, there are
8 relatively few subsequent observations that are influenced by biases imposed towards the end
9 of the optimization window.

10 Figure 5 shows zonally integrated, annual a posteriori emissions from synthetic inversions
11 using surface, CARIBIC, or HIPPO pseudo observations. In each case the state vector for
12 optimization includes monthly emission scale factors on the model grid (but not stratospheric
13 loss rates), and an initial bias of $\pm 50\%$ is applied to emissions in all grid boxes. Results are
14 shown only for the first year of the optimization period since (as shown) the inversion has less
15 ability to retrieve the true emissions in the succeeding months; there are also no HIPPO
16 observations during the last six months of the simulation. As discussed, the surface data
17 provide a good correction to the imposed a priori error in N₂O emissions when starting with
18 both high and low initial biases, and can accurately retrieve zonally integrated emissions in
19 the Northern and Southern Hemispheres.

20 We see in Fig. 5 that inversions based on the HIPPO data are also able to capture the zonal
21 distribution of N₂O emissions. For the high-bias test (a priori emissions scaling factor of 1.5),
22 the inversion results are very similar to those obtained using the surface data. For the low-bias
23 test, the a posteriori emissions retain a low bias over the Southern Ocean, and overshoot
24 slightly where emissions peak in both hemispheres. On the other hand, the CARIBIC
25 measurements lead to substantially different a posteriori fluxes between the high- and low-
26 bias tests: the inversion with the high initial bias returns the true zonal distribution of
27 emissions quite well, whereas the test with the low initial bias leads to an overestimate of
28 emissions from 20° - 30° N and an underestimate elsewhere. We find through these tests that
29 each dataset can independently resolve the global annual flux to within 5% of the true value
30 (Table 3).

1 Based on these experiments, we conclude that relatively sparse observations in the upper
2 troposphere and lowermost stratosphere such as those from CARIBIC are sufficient to correct
3 a prior bias in the global annual N₂O emissions, but do not provide as robust a constraint on
4 the zonal distribution of those emissions. The pole-to-pole HIPPO observations, with their
5 extensive vertical profiling from the upper troposphere to the boundary layer, provide a
6 stronger constraint on the zonal distribution of annual emissions despite the fact that they do
7 not cover the full time period of our optimization. This is because the long lifetime of N₂O
8 allows emissions perturbations to impact concentrations far from source regions 2-6 months
9 after the perturbation (Thompson et al., 2014a). Of the three networks examined here (surface,
10 CARIBIC, and HIPPO) in isolation, the regular surface measurements provide the best
11 correction of annual emission biases.

12 The above OSSEs were performed based on an initial fractional emission bias that is uniform
13 in space and time (i.e., a priori emissions set everywhere to 0.5× or 1.5× the true model
14 values). As we will see later, emission biases that vary in space or time are much more
15 difficult to resolve, due to the sparse observing network combined with the long atmospheric
16 lifetime of N₂O.

17 **5.2 Stratospheric loss of N₂O: Constraints from the observing network and** 18 **impact on source inversions**

19 An important finding from previous work is that N₂O emission estimates derived from surface
20 concentration measurements can be biased by model errors in the stratospheric sink of N₂O
21 (Thompson et al., 2011). Here, we explore the potential for the airborne observations provided
22 by CARIBIC and HIPPO, in conjunction with the surface network, to simultaneously
23 constrain N₂O sinks as well as sources. To this end, we perform a series of synthetic
24 inversions with a prior bias imposed on the stratospheric loss frequencies for N₂O (aggregated
25 to eight equal latitude bands), and assess the degree to which we can correct for errors in the
26 N₂O sink (given a fixed N₂O source) or both the source and sink of N₂O (simultaneously). As
27 previously, a priori scaling factors of either 0.5 or 1.5 are applied in each location and month,
28 and we attempt to retrieve the true value of 1.0 in each case.

29 Figure 6 shows the resulting a posteriori scaling factors for stratospheric loss frequencies
30 when N₂O emissions are held fixed (and equal to their ‘true’ values). We can see that each

1 observational dataset provides some information to correct for biases in the loss frequencies in
2 the first year of the simulation. Stratospheric loss of N₂O in the second (i.e. final) year of the
3 inversion does not significantly affect N₂O mixing ratios at the observation locations, as the
4 timescale for mixing from the upper stratosphere (where most of the N₂O loss occurs) to the
5 troposphere is 1-2 years (Salstein, 1995). As a result, the corresponding a posteriori scale
6 factors do not diverge significantly from their a priori values.

7 For the inversion using surface data, the optimized annual global sink in the first year of the
8 simulation is very close to the true value (Table 3), but the loss frequencies are only adjusted
9 throughout the first year in the tropics. In the extratropics, they adjust primarily during the
10 summer months. The extratropical timing corresponds to the observed seasonal minimum of
11 N₂O at these latitudes (Nevison et al., 2011). At their peaks, retrieved values in the Southern
12 Hemisphere approach the truth, whereas in the Northern Hemisphere they slightly overshoot
13 the true sink. A posteriori values near the poles remain close to the a priori in both
14 hemispheres. Solutions achieved using HIPPO or CARIBIC data are spatially similar to those
15 obtained with the surface observations, although the optimized global sink for both is biased
16 low (by 13-17%, Table 3) due to weaker forcing (fewer total observations, higher observation
17 uncertainty). Therefore, while all the observations provide some correction of biases in the
18 global stratospheric sink of N₂O given known surface fluxes (with the surface data providing
19 the strongest constraint), they provide limited information on the spatial and temporal
20 distribution of that sink.

21 Also shown in Fig. 6 are the a posteriori scaling factors for stratospheric loss frequencies of
22 N₂O when both the source and sink are optimized simultaneously, and given an initial 50%
23 low bias for each. In these tests, the sink does not return to the true value (Table 3); for the
24 inversions using CARIBIC and HIPPO it actually moves slightly in the opposite direction (i.e.
25 further from the truth than the a priori) due to the forcing imposed by the source bias. In other
26 words, the inversion is not able to resolve a bias in N₂O emissions from a bias in the sink.
27 Despite this behavior, the spatial distribution of the derived scaling factors for N₂O emissions
28 (not shown) closely matches that obtained with a fixed ('true') stratospheric sink, and the
29 annual a posteriori emission flux is within 5% of the truth (Table 3) for all tests except the
30 high-bias test using CARIBIC pseudo-data. Therefore, on the 1-2 year timescale of our
31 optimization, and given accurate initial conditions (in our case, based on interpolated

1 measurements), the forcing provided by the surface and aircraft data used here is dominated
2 by N₂O emissions. As a result, a model bias of up to 50% in the stratospheric loss frequencies
3 for N₂O will have minimal impact on the inferred emissions given the inversion framework
4 employed here.

5 Thompson et al. (2011) also examined the feasibility of constraining stratospheric loss rates of
6 N₂O using aircraft observations, but assumed zero model transport error in the observational
7 error covariance matrix. We find that proper treatment of this error has a dramatic effect on
8 the ability of the inversion framework to simultaneously retrieve emissions and stratospheric
9 loss rates of N₂O. In the tests above, the model transport error was estimated based on the
10 variance in N₂O mixing ratios in the grid boxes adjacent to an observation; for aircraft
11 observations near the tropopause, this variability can be an order of magnitude larger than it is
12 near the surface. We find that when we omit the model transport error, the inversion is able to
13 reduce an imposed prior bias in both emissions and stratospheric loss simultaneously, even
14 when those biases have opposing effects on the N₂O burden. As observed above, the same is
15 not true when transport error is accounted for. Our ability to quantify both the emissions and
16 chemistry of N₂O based on aircraft data therefore depends critically on the accuracy of
17 vertical transport in the model, and on the associated transport error assigned in the inversion.
18 Tracer measurements and correlations from platforms such as CARIBIC can be useful for
19 evaluating this.

20 Along with the rate of N₂O destruction in the stratosphere, another factor that can affect N₂O
21 source inversions is model uncertainty in the mass flux of air between the stratosphere and
22 troposphere (e.g., Thompson et al., 2014b). Our model framework, employing assimilated
23 meteorology, is not equipped to include this process directly as part of the state vector for
24 optimization. However, we can explore the relative influence of chemistry versus
25 stratosphere-troposphere mixing on the tropospheric N₂O burden (and hence on N₂O source
26 inversions) with the aid of a simple two-box model representing stratospheric and
27 tropospheric reservoirs of N₂O. Such an analysis does not capture seasonal effects, distinct
28 STE mechanisms operating on different timescales, or spatial gradients within the troposphere
29 and stratosphere, but nonetheless does illustrate some key features of the system.

30 Figure 7 shows the fractional perturbations to the stratospheric and tropospheric burdens of
31 N₂O in the box model that result from: *i*) a 20% increase in the global N₂O emission source

1 (E); *ii*) a 20% decrease in the photochemical loss rate of N_2O (k_{chem}); and *iii*) a 20% decrease
2 in the stratosphere-troposphere exchange rates (k_{ST} and k_{TS}). For the latter, mass fluxes in both
3 directions are increased proportionately since the (annual, global) k_{ST}/k_{TS} ratio is known from
4 the relative sizes of the troposphere and stratosphere.

5 The top panel of Fig. 7 shows that on long timescales a perturbation to k_{ST} and k_{TS} has a
6 negligible effect on the tropospheric N_2O burden compared to a perturbation to k_{chem} or E . A
7 given change in k_{chem} or E leads to a similar relative change in the steady-state burden, with an
8 adjustment timescale dictated by the N_2O lifetime (~ 127 years). In comparison, the effect of a
9 change to k_{TS} and k_{ST} is small in the troposphere. For stratospheric N_2O , the effect of k_{TS} and
10 k_{ST} is somewhat larger and of opposite sign: decreasing k_{TS} and k_{ST} reduces stratospheric N_2O
11 while increasing tropospheric N_2O .

12 However, on short timescales (as is used for our inversions), the importance of stratosphere-
13 troposphere exchange versus chemistry for tropospheric N_2O is reversed, as the former
14 manifests more quickly. The bottom panel of Fig. 7 indicates that for the first 2 years
15 following a perturbation, the effect of k_{TS} and k_{ST} on the tropospheric N_2O burden is $1.3\text{-}29\times$
16 larger (mean: $5.1\times$) than the effect of k_{chem} . Over this same time period, Fig. 7 also shows that
17 the effect of a perturbation to k_{TS} and k_{ST} is significant (mean: $0.8\times$) relative to a change in E .
18 However, the importance of k_{TS} and k_{ST} versus E will be overstated by the box model as it
19 does not resolve spatial gradients within the troposphere or the location of observations
20 relative to emissions.

21 Overall, we can see that N_2O source inversions based on the framework employed here will
22 be unaffected by even relatively large model biases in the chemical loss rate of N_2O . The
23 same does not apply to model biases in STE, and these need to be accounted for when
24 evaluating a posteriori source estimates for N_2O (Thompson et al., 2014b) and other long-
25 lived species such as CO_2 (Deng et al, 2015).

26 **5.3 Temporal resolution of N_2O source inversions**

27 The OSSEs in Sections 5.1 and 5.2 demonstrate that the inversion (and N_2O observing
28 network) has a strong ability to remove model emission biases that are uniform in space and
29 time. However, actual model emission errors are likely to be spatially and temporally

1 dependent. For example, while the a priori natural soil and anthropogenic emissions used here
2 are aseasonal, observations over an agricultural field in Ontario, Canada indicate that 30-90%
3 of the annual flux occurs in the non-growing season, mostly as strong pulses driven by soil
4 thawing (Wagner-Riddle et al., 2007). Likewise, analysis of tall tower observations suggest a
5 strong seasonal cycle of soil N₂O emissions associated with the timing of fertilizer application
6 (Miller et al., 2012; Griffis et al., 2013). A key question, therefore, is the following: At what
7 spatial and temporal resolution can global N₂O emissions be quantified based on the current
8 observing network?

9 To explore the temporal aspect of this question, we performed a test in which we assimilate
10 pseudo observations generated with aseasonal (model truth) emissions while imposing a
11 simple seasonal bias in the a priori emissions from natural and agricultural soils (50% higher
12 than model truth from March – August; 50% lower from September – February). As before,
13 we assimilate surface, CARIBIC, or HIPPO observations, and retrieve monthly scaling factors
14 for terrestrial and oceanic N₂O emissions.

15 Results of this test indicate that a seasonal, global, emission bias is much more difficult to
16 resolve than is a constant bias based on the current network of surface observations. Zonally-
17 integrated emissions (Fig. S2) begin to approach the aseasonal model truth in the Northern
18 Hemisphere during the beginning of the simulation (when the a priori emissions are biased
19 high), but there is almost no correction of the seasonal bias in the latter half of the simulation
20 (when a priori emissions are biased low). Due to the long lifetime of N₂O, any residual high
21 emission bias from the first portion of the simulation leads to positive model-measurement
22 residuals even after the emission bias changes sign. Globally, the result is an annual flux that
23 is biased slightly low (~5%; Table 3) and with incorrect seasonality.

24 In areas near measurement sites, however, some seasonal constraints are afforded in the
25 inversion. For example, Fig. 8 shows monthly fluxes at four locations: a site with continuous
26 observations (KCMP Tall Tower), a site with flask observations (Hegyhátsál, Hungary), a
27 location in eastern China that is upwind of surface flask observations, and a remote site in the
28 Democratic Republic of Congo (DR Congo). At the beginning of the simulation there is a
29 substantial correction of the emission bias at the in situ (KCMP), flask (Hungary), and upwind
30 (East China) sites. During the latter half of the year, when the a priori emissions are biased
31 low, those errors are reduced as a result of the inversion at all three sites, but for the sites with

1 measurements there is a time lag and subsequent overcorrection afterward. There is no
2 significant correction to the biased DR Congo emissions during any point of the year.

3 Based on the above test, we can conclude that flask and in situ observations provide valuable
4 corrections to seasonal emission biases upwind and in the vicinity of the measurements,
5 though not necessarily on a monthly timescale. However, any seasonal biases arising from
6 errors in model STE may be difficult to separate from such seasonal emission errors.
7 Furthermore, large parts of the world (illustrated by the DR Congo site in Fig. 8) lack any
8 meaningful seasonal constraints on emissions.

9 **5.4 Spatial resolution of N₂O source inversions**

10 The spatial resolution at which current measurements constrain global N₂O emissions in this
11 inversion framework can be inferred from the reduction in emission errors that results from
12 the assimilation. Here, we calculate this relative error reduction from a stochastic estimate of
13 the inverse Hessian of the cost function (Eq. 1). For a reasonably linear model, the inverse
14 Hessian approximates the a posteriori error covariance matrix of the emissions, and can be
15 written:

$$16 \quad (\nabla^2 J(\mathbf{x}))^{-1} = (\mathbf{S}_a^{-1} + \mathbf{H}^T \mathbf{S}_y^{-1} \mathbf{H})^{-1} \approx \mathbf{S}_{post} \quad (2)$$

17 where \mathbf{H} is the tangent linear of the forward model, \mathbf{S}_{post} is the a posteriori error covariance
18 matrix, and \mathbf{S}_a and \mathbf{S}_y are the a priori and observational error covariance matrices,
19 respectively, as in Eq. 1. Following Bousserez et al. (2015), we estimate $\nabla^2 J(\mathbf{x})$ using an
20 ensemble (500 members here) of stochastic cost function gradients, each generated by adding
21 Gaussian random noise to the pseudo observations according to the reported uncertainty of
22 each dataset. The reduction in $\mathbf{S}_{post}(i,j)$ relative to $\mathbf{S}_a(i,j)$ for any model grid cell (i,j) then
23 represents the ability of our observing system to remove a random emission error in that
24 location, in the absence of any large-scale source bias.

25 Figure 9 shows the resulting percent error reduction achieved in each model grid cell using
26 surface, CARIBIC, or HIPPO observations for a given month of our two-year simulation.
27 Results using surface observations are shown for month 1 (April 2010), but are comparable
28 for all subsequent months. We see appreciable error reduction near sites with continuous
29 observations in North America and Europe, and more modest error reductions in surrounding

1 grid cells, at sites with flask observations, and in the northern Atlantic upwind of Europe.
2 There is little ($< 5\%$) error reduction achieved throughout the tropics, Southern Hemisphere,
3 and high latitudes, except near Cape Grim, Australia where continuous observations are
4 available. The spatial distribution of the error reduction results is similar to the spatial
5 distribution of scaling factor adjustments in a pseudo observation inversion in which a
6 spatially-random bias has been applied (not shown).

7 Figure 9 also shows that the sparse, high altitude CARIBIC observations provide limited
8 information on the spatial distribution of N_2O emissions. Significant error reduction is
9 achieved over Western Europe during April 2010, the only month in which measurements
10 were taken in the lower troposphere during special flights dedicated to volcano observation
11 (Rauthe-Schöch, 2012). In all other months, measurements occur primarily in the upper
12 troposphere and lower stratosphere and consequently the spatial error reduction is minor
13 (typically $< 1\%$).

14 The spatial information provided by HIPPO observations varies by month according to the
15 flight tracks, and is complementary to that achieved with surface data. For example, during
16 August 2011, we see large error reductions over the central US, as well as some improvement
17 for grid cells in East Asia that are upwind of the HIPPO flight track. Some error reduction is
18 also achieved in these locations for May 2011, despite the fact that no HIPPO flights occurred
19 during this month (the next flights occurred in June). Given the long lifetime of N_2O ,
20 measurements in a given month thus provide some location-specific constraints on emissions
21 in prior months. As is the case with the surface observations, however, the HIPPO data
22 provides very little error reduction for emissions throughout the tropics, Southern Hemisphere
23 and high latitudes. While the OSSE tests above showed that our observation and adjoint
24 framework has significant skill in removing uniform model emission biases, we see in Fig. 9
25 that our current ability to allocate those N_2O emissions spatially around the globe is in fact
26 severely limited relative to the $4^\circ \times 5^\circ$ model resolution used here – and this is true for the
27 airborne as well as the ground-based datasets.

28 Based on the same stochastic approach used above to calculate the inverse Hessian, we can
29 also calculate the averaging kernel of the inversion. The averaging kernel measures the
30 sensitivity of the inversion to emissions in any given grid square; we can thus use it to
31 determine how well emissions in a given location can be independently resolved from

1 emissions elsewhere. If emissions in one location are completely resolved from those in other
2 grid boxes, the averaging kernel value will be 1.0 in that location and 0 everywhere else.
3 Here, we calculate the averaging kernel rows (based on the surface observations only) for a
4 selected group of locations in key emission regions that vary in their proximity to N₂O
5 measurement sites.

6 Figure 10 shows the results for four locations: the KCMP Tall Tower (MN, USA; 44.68° N,
7 93.07 W), Hegyhátsál (Hungary; 46.95° N, 16.65° E), East China (30.0° N, 115.0° E), and the
8 Democratic Republic of Congo (2.0° N, 30.0° E). KCMP features continuous observations,
9 and we see that emissions in this model grid cell can be constrained independently (averaging
10 kernel value near 1.0, and near 0.0 elsewhere) from those in other places. Significant
11 constraints are achieved at Hegyhátsál (averaging kernel value ~0.3), where weekly flask
12 observations are available, though some spatial smearing is apparent. Weaker constraints
13 (averaging kernel values up to ~0.03) are achieved in the vicinity of the East China grid box,
14 likely provided by downwind observations in Korea and the western Pacific.

15 Averaging kernel values for the Central Africa location are very low ($\sim 10^{-3}$), indicating little
16 to no constraint on the source flux, and are also highly smeared spatially, showing that the
17 current surface observations of N₂O do not allow emissions in that region to be independently
18 resolved from emissions elsewhere across the globe. We see in Fig. 10 that this spatial
19 smearing even extends to the midlatitudes in both hemispheres. Emissions in the
20 underconstrained tropics thus risk being conflated with those in other, distant source regions
21 in global inversion analyses.

22 The implications of this current lack of constraints on tropical N₂O emissions can be seen in a
23 sample global inversion based on real atmospheric data. Figure 11 shows a posteriori emission
24 scaling factors for global inversions based on two different assumptions: the first uses our
25 previous construction of the a priori error covariance matrix (100% uncertainty with
26 horizontal correlation length scales of 500 km over land and 1000 km over ocean); the other
27 does not include any penalty term (measuring the departure from a priori conditions) in the
28 cost function. When a priori constraints are included, the solution is relatively spatially
29 smooth. To correct for a low bias in our a priori emissions inventory, emissions increase
30 throughout those terrestrial and oceanic regions where emissions occur, with a slightly higher
31 inferred flux over South America. Conversely, when we eliminate the a priori constraint,

1 emissions increase strongly in the tropics and Southern Hemisphere, reaching a factor of 10
2 (the upper bound placed on the scaling factors) in South America near the beginning of the
3 two-year simulation. To compensate for this, the inferred emissions throughout the Northern
4 Hemisphere decrease dramatically.

5 This severe sensitivity of the solution to the a priori error assumption reflects the ill-posed
6 nature of the problem. It also highlights the fact that, because the global N₂O flux is
7 constrained (as the N₂O lifetime and atmospheric burden are reasonably well-known), the lack
8 of constraint on tropical emissions has important implications for understanding emissions
9 elsewhere in the world.

10 **5.5 Identifying priority locations for future N₂O measurements**

11 In this section, we apply the error reduction statistics derived above to identify priority regions
12 where new observations are likely to have high value for improving present understanding of
13 global N₂O sources. To that end, we carry out forward model simulations in which N₂O
14 emissions in the first month are scaled by $(1 - x)$, where x is the spatial map of relative error
15 reductions achieved in the inversion on the basis of the surface observations (e.g., Fig. 9). The
16 initial atmospheric burden of N₂O is set to zero, as are the emissions in subsequent months.
17 The resulting atmospheric N₂O then reflects unconstrained emissions, and the distribution of
18 that ‘unconstrained N₂O’ in space and time shows where new observations are needed to
19 quantify those emissions in a spatially explicit way.

20 Figure 12 shows the distribution of unconstrained N₂O mapped in the first and the second
21 month following its emission. Results are shown for simulations starting in August 2010 and
22 February 2011; these months were chosen to illustrate how seasonal differences in horizontal
23 and vertical transport affect the atmospheric dispersion of underconstrained N₂O emissions. In
24 August, unconstrained mixing ratios above 1 ppb can be found throughout Southeast Asia,
25 Central Africa, and South America, with the highest concentrations occurring over Brazil and
26 off the western coasts of Africa and South America. Somewhat elevated concentrations (0.5-1
27 ppb) persist in these locations for the second month of the simulation, but these become well-
28 dispersed in the following months (not shown). Unconstrained N₂O emitted in August is
29 initially concentrated in the lower troposphere in the tropics and northern midlatitudes, but is
30 lofted through the tropical troposphere by September. In contrast, unconstrained N₂O emitted

1 in February is more strongly confined to the lower troposphere and the Northern Hemisphere,
2 even a month after emission.

3 The maps in Fig. 12 rely by necessity on a particular a priori estimate of N₂O emissions and
4 their distribution in space and time. However, they nonetheless provide an assessment of
5 where additional measurements would have the best leverage for improving N₂O emission
6 estimates, based on our existing bottom-up understanding of when and where those emissions
7 occur. We see in the maps that areas over or downwind of the tropics and East Asia should
8 receive the highest measurement priority to reduce uncertainty in the overall N₂O budget. As
9 shown earlier, downwind surface observations can provide some spatially explicit emission
10 constraints for regions with high fluxes; these may be the only feasible option for places
11 where access, infrastructure, or political issues prevent sustained local measurements. We
12 note that additional N₂O measurements are now available in and around Japan (Saikawa et al.,
13 2013) that may provide additional constraints on East Asian emissions not achieved using the
14 measurements presented here. In addition, aircraft measurements during the July-September
15 timeframe should have strong value for constraining fluxes in the tropics, given the lofting
16 and dispersal of those emissions that is apparent in the August 2010 simulation. The value of
17 such measurements was also pointed out by Kort et al. (2011), who reported observational
18 evidence for lofting of large, episodic tropical emissions. On the other hand, Fig. 12 also
19 reveals large areas of the world's oceans where additional surface measurements are not likely
20 to provide appreciable new insights into the global N₂O budget, given the lack of
21 unconstrained N₂O that is less than 1-2 months from emission.

22

23 **6 Summary and conclusions**

24 We developed a new inversion framework based on the GEOS-Chem model and its adjoint
25 for estimating global N₂O emissions and stratospheric loss rates using surface (flask and in-
26 situ) as well as airborne (CARIBIC; HIPPO) measurements. We used this framework to: *i*)
27 quantify the ability of the current observing network to constrain the global distribution of
28 N₂O sources and sinks; *ii*) assess the relative utility of the various observing platforms for
29 doing so; and *iii*) identify priority locations where measurements are most needed to improve
30 present understanding of the N₂O budget. Our simulation period runs from April 2010 to

1 April 2012, with initial conditions constructed using surface flask observations and vertical
2 profile measurements from the MLS satellite sensor.

3 Observing system simulation experiments (OSSEs) showed that the surface and HIPPO
4 observations can accurately resolve a uniform bias in N₂O emissions for the first year of a
5 two-year simulation; in comparison, the sparser (and mostly high altitude) CARIBIC
6 observations provide a weaker constraint. All three datasets are able to independently resolve
7 the global surface flux to within 5% of the truth. On the other hand, a seasonal emission bias
8 is much more difficult to resolve given the long lifetime of N₂O, particularly in regions with
9 sparse observations. The surface observations do provide a reduction of seasonal emission
10 errors in the vicinity of measurement sites and in large source regions upwind.

11 The surface and airborne datasets are all able to resolve a global bias in the stratospheric loss
12 rate of N₂O given known emissions, but do not give information on the spatial and temporal
13 distribution of that sink. For the more realistic scenario with uncertain N₂O sources and sink,
14 we find that resolving the two in a joint source-sink inversion would require greater
15 confidence in modeled transport than is currently warranted. Nevertheless, because of the
16 timescale for stratosphere-troposphere mixing, N₂O source inversions are insensitive to
17 uncertainties in the chemical sink of N₂O on the 2 year analysis time frame used here (and
18 assuming an accurate initial state; e.g. from interpolated data). However, a simple box model
19 analysis shows that tropospheric N₂O is more sensitive to uncertainties in the rate of
20 stratosphere-troposphere exchange (STE) than to those in the chemical loss rates for analysis
21 timescales up to ~3-4 years. Incomplete knowledge of STE rates will thus be a key source of
22 uncertainty to address for N₂O source inversions on these timescales.

23 We employed a stochastic estimate of the inverse Hessian to quantify the spatial resolution of
24 N₂O emission constraints afforded by the current global network of observations, and the
25 degree to which emissions in a particular location can be distinguished from those elsewhere.
26 Significant location-specific constraints are achieved in grid boxes near and immediately
27 upwind of surface observation locations; however, these are mainly confined to North
28 America, Europe and Australia. For sites with continuous surface observations, local
29 emissions can be unambiguously resolved from those in surrounding locations, as indicated
30 by large error reductions and averaging kernel (AK) values close to 1.0. Flask observations
31 also provide significant local-to-regional constraints (e.g., AK values of ~0.3 at a site with

1 weekly measurements). HIPPO observations primarily provide emission constraints for the
2 Central US and East Asia. Critically, little to no spatial information on tropical emissions is
3 provided by either set of observations: the corresponding AKs are highly smeared spatially
4 and show that emissions in many parts of the tropics cannot even be resolved from those in
5 the midlatitudes. For global inversions, this underconstraint in the tropics can thus lead to
6 large errors in the inferred N₂O fluxes for the extratropics as well as the tropics themselves.

7 From the atmospheric distribution of ‘unconstrained N₂O’ simulated based on the error
8 reduction statistics achieved in the inversion and our a priori source estimates, we identify
9 areas in the tropics and East Asia as the highest priorities for new N₂O measurements to
10 advance understanding of the global budget. In situ or flask observations downwind of major
11 sources in South America, Central Africa, and East Asia can provide some spatial information
12 on N₂O fluxes in cases where local, long-term measurements are impractical. Targeted aircraft
13 measurements in the troposphere could also provide much-needed constraints on tropical
14 emission fluxes, particularly during July-September when emissions are well-lofted vertically.

15 From our analysis it is clear that additional measurements are crucial to obtaining a more
16 complete picture of global N₂O sources, particularly in the key areas mentioned above. In this
17 context, we will further investigate the use of efficient randomization techniques to estimate
18 the spatiotemporal constraints provided by new and existing N₂O measurements, and design
19 optimal dimension approaches for N₂O source inversions. Such work could also include an
20 evaluation of information provided by new N₂O retrievals from AIRS (Xiong et al., 2014) and
21 other space-based infrared sounders. While the vertical sensitivity of such instruments may be
22 insufficient to derive useful direct information on surface emissions, such data could be useful
23 for constraining the N₂O profile and its stratosphere-troposphere exchange (thus indirectly
24 improving our ability to diagnose sources). The fact that the current observing system yields
25 little information on the space-time distribution of N₂O fluxes over large parts of the world
26 also speaks to the need for process-based emission models that can provide a priori source
27 estimates that faithfully capture the key modes of variability. Such models are also needed to
28 project how soil N₂O fluxes will respond to future changes in climate, hydrology, and
29 nitrogen deposition and runoff.

30

31 **Acknowledgments**

1 This work was supported by NOAA (grant no. NA13OAR4310086) and the Minnesota
2 Supercomputing Institute. We thank J. Muhle and C. Harth (UCSD-SIO), D. Young (U.
3 Bristol), P. Fraser (CSIRO), R. Wang (GaTech), and other members of the AGAGE team for
4 providing AGAGE data. The 6 AGAGE stations used here are supported principally by
5 NASA (USA) grants to MIT and SIO, and also by DECC (UK) and NOAA (USA) grants to
6 Bristol University, and by CSIRO and BoM (Australia). We thank Environment Canada for
7 providing data from the Churchill, Estevan Point, East Trout Lake, Fraserdale, and Sable
8 Island sites. We thank R. Martin and S. Nichol for providing data from the Arrival Heights
9 NIWA station.

10

11 **Code availability**

12 The N₂O version of the GEOS-Chem adjoint code is available via the GEOS-Chem adjoint
13 repository. Instructions for obtaining access to the code can be found at
14 wiki.seas.harvard.edu/geos-chem/index.php/GEOS-Chem_Adjoint.

15

16 **References**

17 Assonov, S. S., Brenninkmeijer, C. A. M., Schuck, T., and Umezawa, T.: N₂O as a tracer of
18 mixing stratospheric and tropospheric air based on CARIBIC data with applications for CO₂,
19 *Atmos. Environ.*, 79, 769-779, doi:10.1016/j.atmosenv.2013.07.035, 2013.

20 Bousserez, N., Henze, D. K., Perkins, A., Bowman, K. W., Lee, M., Liu, J., Deng, F., and
21 Jones, D. B. A., Improved analysis-error covariance matrix for high-dimensional variational
22 inversions: application to source estimation using a 3D atmospheric transport model, *Q. J.*
23 *Roy. Meteor. Soc.*, doi:10.1002/qj.2495, 2015.

24 Bouwman, A. F.: Environmental science - Nitrogen oxides and tropical agriculture, *Nature*,
25 392, 866-867, doi:10.1038/31809, 1998.

26 Bouwman, A. F., Beusen, A. H. W., Griffioen, J., Van Groenigen, J. W., Hefting, M. M.,
27 Oenema, O., Van Puijenbroek, P. J. T. M., Seitzinger, S., Slomp, C. P., and Stehfest, E.:
28 Global trends and uncertainties in terrestrial denitrification and N₂O emissions, *Philos. T. Roy*
29 *Soc. B*, 368, 20130112, doi:10.1098/rstb.2013.0112, 2013.

1 Brennkmeijer, C. A. M., Crutzen, P., Boumard, F., Dauer, T., Dix, B., Ebinghaus, R.,
2 Filippi, D., Fischer, H., Franke, H., Friess, U., Heintzenberg, J., Helleis, F., Hermann, M.,
3 Kock, H. H., Koeppel, C., Lelieveld, J., Leuenberger, M., Martinsson, B. G., Miemczyk, S.,
4 Moret, H. P., Nguyen, H. N., Nyfeler, P., Oram, D., O'Sullivan, D., Penkett, S., Platt, U.,
5 Pupek, M., Ramonet, M., Randa, B., Reichelt, M., Rhee, T. S., Rohwer, J., Rosenfeld, K.,
6 Scharffe, D., Schlager, H., Schumann, U., Slemr, F., Sprung, D., Stock, P., Thaler, R.,
7 Valentino, F., van Velthoven, P., Waibel, A., Wandel, A., Waschitschek, K., Wiedensohler,
8 A., Xueref-Remy, I., Zahn, A., Zech, U., and Ziereis, H.: Civil Aircraft for the regular
9 investigation of the atmosphere based on an instrumented container: The new CARIBIC
10 system, *Atmos. Chem. Phys.*, 7, 4953-4976, doi:10.5194/acp-7-4953-2007, 2007.

11 Butterbach-Bahl, K., Baggs, E. M., Dannenmann, M., Kiese, R., and Zechmeister-Boltenstern,
12 S.: Nitrous oxide emissions from soils: how well do we understand the processes and their
13 controls?, *Philos. T. Roy Soc. B*, 368, 20140122, doi:10.1098/rstb.2013.0122, 2013.

14 Byrd, R. H., Lu, P. H., Nocedal, J., and Zhu, C. Y.: A limited memory algorithm for bound
15 constrained optimization, *SIAM J. Sci. Comput.*, 16, 1190-1208, doi:10.1137/0916069, 1995.

16 Cohen, Y., and Gordon, L. I.: Nitrous oxide production in the ocean, *J. Geophys. Res.-Oc.*
17 *Atm.*, 84, 347-353, doi:10.1029/JC084iC01p00347, 1979.

18 Cooper, L. N., Steele, L. P., Langenfelds, R. L., Spencer, D. A., and Lucarelli, M. P.:
19 Atmospheric methane, carbon dioxide, hydrogen, carbon monoxide and nitrous oxide from
20 Cape Grim flask air samples analysed by gas chromatography, *Baseline Atmospheric Program*
21 (Australia) 1996, 98 - 102, Bureau of Meteorology and CSIRO Atmospheric Research, 1999.

22 Davidson, E. A.: The contribution of manure and fertilizer nitrogen to atmospheric nitrous
23 oxide since 1860, *Nat. Geosci.*, 2, 659-662, doi:10.1038/ngeo608, 2009.

24 Deng, F., Jones, D. B. A., Walker, T. W., Keller, M., Bowman, K. W., Henze, D. K., Nassar,
25 R., Kort, E. A., Wofsy, S. C., Walker, K. A., Bourassa, A. E., and Degenstein, D. A.:
26 Sensitivity analysis of the potential impact of discrepancies in stratosphere-troposphere
27 exchange on inferred sources and sinks of CO₂, *Atmos. Chem. Phys. Discuss.*, 15, 10813-
28 10851, doi:10.5194/acpd-15-10813-2015, 2015.

29 Denman, K. L., Brasseur, G. P., Chidthaisong, A., Ciais, P., Cox, P. M., Dickinson, R. E.,
30 Hauglustaine, D., Heinze, C., Holland, E., Jacob, D., Lohmann, U., Ramachandran, S., da

1 Silva Dias, P. L., Wofsy, S. C., and Zhang, X.: Couplings Between Changes in the Climate
2 System and Biogeochemistry, in: *Climate Change 2007: Contribution of Working Group I to*
3 *the Fourth Assessment Report of the Intergovernmental Panel on Climate Change*, edited by:
4 Solomon, S. D., Qin, D., Manning, M., Chen, Z., Marquis, M., Averyt, K. B., Tignor, M., and
5 Miller, H. L., Cambridge University Press, Cambridge, 499-587, 2007.

6 Dlugokencky, E. J., Steele, L. P., Lang, P. M., and Masarie, K. A.: The growth rate and
7 distribution of atmospheric methane, *J. Geophys. Res.-Atmos.*, 99, 17021-17043,
8 doi:10.1029/94JD01245, 1994.

9 Firestone, M. K., and Davidson, E. A.: Microbiological basis of NO and N₂O production and
10 consumption in the soil, in: *Exchange of Trace Gases Between Terrestrial Ecosystems and the*
11 *Atmosphere*, edited by: Andreae, M. O., and Schimel, D. S., Wiley and Sons, Chichester, 7-
12 21, 1989.

13 Forster, P., Ramaswamy, V., Artaxo, P., Berntsen, T., Betts, R., Fahey, D. W., Haywood, J.,
14 Lean, J., Lowe, D. C., Myrhe, G., Nganga, J., Prinn, R., Raga, G., Schulz, M., and Van
15 Doorland, R.: *Changes in atmospheric constituents and in radiative forcing*, Cambridge,
16 United Kingdom, and New York, NY, USA, 2007.

17 Elkins, J. W., Wofsy, S. C., McElroy, M. B., Kolb, C. E., and Kaplan, W. A.: Aquatic sources
18 and sinks for nitrous oxide, *Nature*, 275, 602-606, 1978.

19 Francey, R. J., Steele, L. P., Langenfelds, R. L., Lucarelli, M. P., Allison, C. E., Beardsmore,
20 D. J., Coram, S. A., Derek, N., de Silva, F. R., Etheridge, D. M., Fraser, P. J., Henry, R. J.,
21 Turner, B., Welch, E. D., Spencer, D. A., and Cooper, L. N.: *Global Atmospheric Sampling*
22 *Laboratory (GASLAB): supporting and extending the Cape Grim trace gas programs,*
23 *Baseline Atmospheric Program (Australia) 1993*, 8-29, Bureau of Meteorology and CSIRO
24 division of Atmospheric Research, 1996.

25 Galloway, J. N., Townsend, A. R., Erisman, J. W., Bekunda, M., Cai, Z. C., Freney, J. R.,
26 Martinelli, L. A., Seitzinger, S. P., and Sutton, M. A.: Transformation of the nitrogen cycle:
27 Recent trends, questions, and potential solutions, *Science*, 320, 889-892,
28 doi:10.1126/science.1136674, 2008.

29 Griffis, T. J., Lee, X., Baker, J. M., Russelle, M. P., Zhang, X., Venterea, R., and Millet, D.
30 B.: Reconciling the differences between top-down and bottom-up estimates of nitrous oxide

1 emissions for the US Corn Belt, *Global Biogeochem. Cy.*, 27, 746-754,
2 doi:10.1002/gbc.20066, 2013.

3 Henze, D. K., Hakami, A., and Seinfeld, J. H.: Development of the adjoint of GEOS-Chem,
4 *Atmos. Chem. Phys.*, 7, 2413-2433, doi:10.5194/acp-7-4953-2007, 2007.

5 Henze, D. K., Seinfeld, J. H., and Shindell, D. T.: Inverse modeling and mapping US air
6 quality influences of inorganic PM_{2.5} precursor emissions using the adjoint of GEOS-Chem,
7 *Atmos. Chem. Phys.*, 9, 5877-5903, doi:10.5194/acp-9-5877-2009, 2009.

8 Hirsch, A. I., Michalak, A. M., Bruhwiler, L. M., Peters, W., Dlugokencky, E. J., and Tans, P.
9 P.: Inverse modeling estimates of the global nitrous oxide surface flux from 1998-2001,
10 *Global Biogeochem. Cy.*, 20, GB1008, 17, doi:10.1029/2004gb002443, 2006.

11 Huang, J., Golombek, A., Prinn, R., Weiss, R., Fraser, P., Simmonds, P., Dlugokencky, E. J.,
12 Hall, B., Elkins, J., Steele, P., Langenfelds, R., Krummel, P., Dutton, G., and Porter, L.,
13 Estimation of regional emissions of nitrous oxide from 1997 to 2005 using multinetwork
14 measurements, a chemical transport model, and an inverse method, *J. Geophys. Res.*, 113,
15 D17313, doi:10.1029/2007JD009381, 2008.

16 IPCC: 2006 IPCC Guidelines for National Greenhouse Gas Inventories, edited by: Eggleston,
17 H. S., Buendia, L., Miwa, K., Ngara, T., and Tanabe, K., IGES, Japan, 2006.

18 Jiang, Z., Jones, D. B. A., Kopacz, M., Liu, J., Henze, D. K., and Heald, C.: Quantifying the
19 impact of model errors on top-down estimates of carbon monoxide emissions using satellite
20 observations, *J. Geophys. Res.-Atmos.*, 116, D15306, doi:10.1029/2010JD015282, 2011.

21 Jiang, Z., Jones, D. B. A., Worden, H. M., Deeter, M. N., Henze, D. K., Worden, J., Bowman,
22 K. W., Brenninkmeijer, C. A. M., and Schuck, T. J.: Impact of model errors in convective
23 transport on CO source estimates inferred from MOPITT CO retrievals, *J. Geophys. Res.*,
24 118, 2073-2083, doi:10.1002/jgrd.50216, 2013.

25 Jin, X., and Gruber, N.: Offsetting the radiative benefit of ocean iron fertilization by
26 enhancing N₂O emissions, *Geophys. Res. Lett.*, 30, 2249, doi:10.1029/2003GL018458, 2003.

27 Kopacz, M., Jacob, D. J., Henze, D. K., Heald, C. L., Streets, D. G., and Zhang, Q.:
28 Comparison of adjoint and analytical Bayesian inversion methods for constraining Asian

1 sources of carbon monoxide using satellite (MOPITT) measurements of CO columns, J.
2 Geophys. Res.-Atmos., 114, D04305, doi:10.1029/2007JD009264, 2009.

3 Kopacz, M., Jacob, D. J., Fisher, J. A., Logan, J. A., Zhang, L., Megretskaia, I. A., Yantosca,
4 R. M., Singh, K., Henze, D. K., Burrows, J. P., Buchwitz, M., Khlystova, I., McMillan, W.
5 W., Gille, J. C., Edwards, D. P., Eldering, A., Thouret, V., and Nedelec, P.: Global estimates
6 of CO sources with high resolution by adjoint inversion of multiple satellite datasets
7 (MOPITT, AIRS, SCIAMACHY, TES), Atmos. Chem. Phys., 10, 855-876, doi:10.5194/acp-
8 10-855-2010, 2010.

9 Kopacz, M., Mauzerall, D. L., Wang, J., Leibensperger, E. M., Henze, D. K., and Singh, K.:
10 Origin and radiative forcing of black carbon transported to the Himalayas and Tibetan
11 Plateau, Atmos. Chem. Phys., 11, 2837-2852, doi:10.5194/acp-11-2837-2011, 2011.

12 Kort, E. A., Patra, P. K., Ishijima, K., Daube, B. C., Jimenez, R., Elkins, J., Hurst, D., Moore,
13 F. L., Sweeney, C., Wofsy, S. C.: Tropospheric distribution and variability of N₂O: Evidence
14 for strong tropical emissions, Geophys. Res. Lett., 38, L15806, doi:10.1029/2011GL047612,
15 2011.

16 Lambert, A., Read, W. G., Livesey, N. J., Santee, M. L., Manney, G. L., Froidevaux, L., Wu,
17 D. L., Schwartz, M. J., Pumphrey, H. C., Jimenez, C., Nedoluha, G. E., Cofield, R. E., Cuddy,
18 D. T., Daffer, W. H., Drouin, B. J., Fuller, R. A., Jarnot, R. F., Knosp, B. W., Pickett, H. M.,
19 Perun, V. S., Snyder, W. V., Stek, P. C., Thurstans, R. P., Wagner, P. A., Waters, J. W.,
20 Jucks, K. W., Toon, G. C., Stachnik, R. A., Bernath, P. F., Boone, C. D., Walker, K. A.,
21 Urban, J., Murtagh, D., Elkins, J. W., and Atlas, E.: Validation of the Aura Microwave Limb
22 Sounder middle atmosphere water vapor and nitrous oxide measurements, J. Geophys. Res.-
23 Atmos., 112, D24S36, doi:10.1029/2007JD008724, 2007.

24 Law, C. S., and Owens, N. J. P.: Significant flux of atmospheric nitrous oxide from the
25 northwest Indian Ocean, Nature, 346, 826-828, doi:10.1038/346826a0, 1990.

26 Maggioro, S. R., Webb, J. A., Wagner-Riddle, C., and Thurtell, G. W.: Nitrous and nitrogen
27 oxide emissions from turfgrass receiving different forms of nitrogen fertilizer, J. Environ.
28 Qual., 29, 621-630, 2000.

29 Miller, S. M., Kort, E. A., Hirsch, A. I., Dlugokencky, E. J., Andrews, A. E., Xu, X., Tian, H.,
30 Nehr Korn, T., Eluszkiewicz, J., Michalak, A. M., and Wofsy, S. C.: Regional sources of

1 nitrous oxide over the United States: Seasonal variation and spatial distribution, *J. Geophys.*
2 *Res.-Atmos.*, 117, D06310, doi:10.1029/2011JD016951, 2012.

3 Mosier, A., Kroeze, C., Nevison, C., Oenema, O., Seitzinger, S., and van Cleemput, O.:
4 Closing the global N₂O budget: nitrous oxide emissions through the agricultural nitrogen
5 cycle - OECD/IPCC/IEA phase II development of IPCC guidelines for national greenhouse
6 gas inventory methodology, *Nutr. Cycl. Agroecosys.*, 52, 225-248,
7 doi:10.1023/a:1009740530221, 1998.

8 Nevison, C. D., Keeling, R. F., Weiss, R. F., Popp, B. N., Jin, X., Fraser, P. J., Porter, L. W.,
9 and Hess, P. G.: Southern Ocean ventilation inferred from seasonal cycles of atmospheric
10 N₂O and O₂/N₂ at Cape Grim, Tasmania, *Tellus B*, 57, 218-229, doi:10.1111/j.1600-
11 0889.2005.00143.x, 2005.

12 Nevison, C. D., Dlugokencky, E., Dutton, G., Elkins, J. W., Fraser, P., Hall, B., Krummel, P.
13 B., Langenfelds, R. L., O'Doherty, S., Prinn, R. G., Steele, L. P., and Weiss, R. F.: Exploring
14 causes of interannual variability in the seasonal cycles of tropospheric nitrous oxide, *Atmos.*
15 *Chem. Phys.*, 11, 3713-3730, doi:10.5194/acp-11-3713-2011, 2011.

16 Park, S., Croteau, P., Boering, K. A., Etheridge, D. M., Ferretti, D., Fraser, P. J., Kim, K. R.,
17 Krummel, P. B., Langenfelds, R. L., van Ommen, T. D., Steele, L. P., and Trudinger, C. M.:
18 Trends and seasonal cycles in the isotopic composition of nitrous oxide since 1940, *Nat.*
19 *Geosci.*, 5, 261-265, doi:10.1038/ngeo1421, 2012.

20 Parrington, M., Palmer, P. I., Henze, D. K., Tarasick, D. W., Hyer, E. J., Owen, R. C.,
21 Helmig, D., Clerbaux, C., Bowman, K. W., Deeter, M. N., Barratt, E. M., Coheur, P. F.,
22 Hurtmans, D., Jiang, Z., George, M., and Worden, J. R.: The influence of boreal biomass
23 burning emissions on the distribution of tropospheric ozone over North America and the
24 North Atlantic during 2010, *Atmos. Chem. Phys.*, 12, 2077-2098, doi:10.5194/acp-12-2077-
25 2012, 2012.

26 Potter, C. S., Matson, P. A., Vitousek, P. M., and Davidson, E. A.: Process modeling of
27 controls on nitrogen trace gas emissions from soils worldwide, *J. Geophys. Res.-Atmos.*, 101,
28 1361-1377, doi:10.1029/95JD02028, 1996.

1 Prather, M. J., Holmes, C. D., and Hsu, J.: Reactive greenhouse gas scenarios: Systematic
2 exploration of uncertainties and the role of atmospheric chemistry, *Geophys. Res. Lett.*, 39,
3 L09803, doi:10.1029/2012GL051440, 2012.

4 Prinn, R. G., Weiss, R. F., Fraser, P. J., Simmonds, P. G., Cunnold, D. M., Alyea, F. N.,
5 O'Doherty, S., Salameh, P., Miller, B. R., Huang, J., Wang, R. H. J., Hartley, D. E., Harth, C.,
6 Steele, L. P., Sturrock, G., Midgley, P. M., and McCulloch, A.: A history of chemically and
7 radiatively important gases in air deduced from ALE/GAGE/AGAGE, *J. Geophys. Res.*, 105,
8 17751-17792, doi:10.1029/2000JD900141, 2000.

9 Rauthe-Schöch, A., Weigelt, A., Hermann, M., Martinsson, B. G., Baker, A. K., Heue, K. P.,
10 Brenninkmeijer, C. A. M., Zahn, A., Scharffe, D., Eckhardt, S.: CARIBIC aircraft
11 measurements of Eyjafjallajökull volcanic clouds in April/May 2010, *Atmos. Chem. Phys.*,
12 12, 879-902, 10.5194/acp-12-879-2012, 2012.

13 Ravishankara, A. R., Daniel, J. S., and Portmann, R. W.: Nitrous Oxide (N₂O): The Dominant
14 Ozone-Depleting Substance Emitted in the 21st Century, *Science*, 326, 123-125,
15 doi:10.1126/science.1176985, 2009.

16 Saikawa, E., Prinn, R. G., Dlugokencky, E., Ishijima, K., Dutton, G. S., Hall, B. D.,
17 Langenfelds, R., Tohjima, Y., Machida, T., Manizza, M., Rigby, M., O'Doherty, S., Patra, P.
18 K., Harth, C. M., Weiss, R. F., Krummel, P. B., van der Schoot, M., Fraser, P. J., Steele, L. P.,
19 Aoki, S., Nakazawa, T., and Elkins, J. W.: Global and regional emissions estimates for N₂O,
20 *Atmos. Chem. Phys.*, 14, 4617-4641, doi:10.5194/acp-14-4617-2014, 2014.

21 Salstein, D. A.: Mean properties of the atmosphere, in: *Composition, Chemistry, and Climate*
22 *of the Atmosphere*, edited by: Singh, H. B., Van Nostrand Reinhold, New York, 19-49, 1995.

23 Schuck, T. J., Brenninkmeijer, C. A. M., Slemr, F., Xueref-Remy, I., and Zahn, A.:
24 Greenhouse gas analysis of air samples collected onboard the CARIBIC passenger aircraft,
25 *Atmos. Meas. Tech.*, 2, 449-464, doi:10.5194/amt-2-449-2009, 2009.

26 Shcherbak, I., Millar, N., and Robertson, G. P.: Global metaanalysis of the nonlinear response
27 of soil nitrous oxide (N₂O) emissions to fertilizer nitrogen, *P. Natl. Acad. Sci. USA*, 111,
28 9199-9204, doi:10.1073/pnas.1322434111, 2014.

1 Thompson, R. L., Bousquet, P., Chevallier, F., Rayner, P. J., and Ciais, P.: Impact of the
2 atmospheric sink and vertical mixing on nitrous oxide fluxes estimated using inversion
3 methods, *J. Geophys. Res.-Atmos.*, 116, D17307, doi:10.1029/2011JD015815, 2011.

4 Thompson, R. L., Chevallier, F., Crotwell, A. M., Dutton, G., Langenfelds, R. L., Prinn, R.
5 G., Weiss, R. F., Tohjima, Y., Nakazawa, T., Krummel, P. B., Steele, L. P., Fraser, P.,
6 O'Doherty, S., Ishijima, K., and Aoki, S.: Nitrous oxide emissions 1999 to 2009 from a global
7 atmospheric inversion, *Atmos. Chem. Phys.*, 14, 1801-1817, doi:10.5194/acp-14-1801-2014,
8 2014a.

9 Thompson, R. L., Patra, P. K., Ishijima, K., Saikawa, E., Corazza, M., Karstens, U., Wilson,
10 C., Bergamaschi, P., Dlugokencky, E., Sweeney, C., Prinn, R. G., Weiss, R. F., O'Doherty, S.,
11 Fraser, P. J., Steele, L. P., Krummel, P. B., Saunio, M., Chipperfield, M., and Bousquet, P.:
12 TransCom N₂O model inter-comparison - Part 1: Assessing the influence of transport and
13 surface fluxes on tropospheric N₂O variability, *Atmos. Chem. Phys.*, 14, 4349-4368,
14 doi:10.5194/acp-14-4349-2014, 2014b.

15 Thompson, R. L., Ishijima, K., Saikawa, E., Corazza, M., Karstens, U., Patra, P. K.,
16 Bergamaschi, P., Chevallier, F., Dlugokencky, E., Prinn, R. G., Weiss, R. F., O'Doherty, S.,
17 Fraser, P. J., Steele, L. P., Krummel, P. B., Vermeulen, A., Tohjima, Y., Jordan, A., Haszpra,
18 L., Steinbacher, M., Van der Laan, S., Aalto, T., Meinhardt, F., Popa, M. E., Moncrieff, J.,
19 and Bousquet, P.: TransCom N₂O model inter-comparison - Part 2: Atmospheric inversion
20 estimates of N₂O emissions, *Atmos. Chem. Phys.*, 14, 6177-6194, doi:10.5194/acp-14-6177-
21 2014, 2014c.

22 Umezawa, T., Baker, A. K., Oram, D., Sauvage, C., O'Sullivan, D., Rauthe-Schoch, A.,
23 Montzka, S. A., Zahn, A., Brenninkmeijer, C. A. M.: Methyl chloride in the upper troposphere
24 observed by CARIBIC passenger aircraft observatory: Large-scale distributions and Asian
25 summer monsoon outflow, *J. Geophys. Res.-Atmos.*, 119, 5542-5558,
26 doi:10.1002/2013JD021396, 2014.

27 van der Werf, G. R., Randerson, J. T., Giglio, L., Collatz, G. J., Mu, M., Kasibhatla, P. S.,
28 Morton, D. C., DeFries, R. S., Jin, Y., and van Leeuwen, T. T.: Global fire emissions and the
29 contribution of deforestation, savanna, forest, agricultural, and peat fires (1997-2009), *Atmos.*
30 *Chem. Phys.*, 10, 11707-11735, doi:10.5194/acp-10-11707-2010, 2010.

1 Volk, C. M., Elkins, J. W., Fahey, D. W., Dutton, G. S., Gilligan, J. M., Loewenstein, M.,
2 Podolske, J. R., Chan, K. R., and Gunson, M. R.: Evaluation of source gas lifetimes from
3 stratospheric observations, *J. Geophys. Res.-Atmos.*, 102, 25543-25564,
4 doi:10.1029/97JD02215, 1997.

5 Wagner-Riddle, C., Furon, A., McLaughlin, N. L., Lee, I., Barbeau, J., Jayasundara, S.,
6 Parkin, G., Von Bertoldi, P., and Warland, J.: Intensive measurement of nitrous oxide
7 emissions from a corn-soybean-wheat rotation under two contrasting management systems
8 over 5 years, *Glob. Change Biol.*, 13, 1722-1736, doi:10.1111/j.1365-2486.2007.01388.x,
9 2007.

10 Wang, J., Xu, X., Henze, D. K., Zeng, J., Ji, Q., Tsay, S.-C., and Huang, J.: Top-down
11 estimate of dust emissions through integration of MODIS and MISR aerosol retrievals with
12 the GEOS-Chem adjoint model, *Geophys. Res. Lett.*, 39, L08802,
13 doi:10.1029/2012GL051136, 2012.

14 Wells, K. C., Millet, D. B., Cady-Pereira, K. E., Shephard, M. W., Henze, D. K., Bousserrez,
15 N., Apel, E. C., de Gouw, J., Warneke, C., and Singh, H. B.: Quantifying global terrestrial
16 methanol emissions using observations from the TES satellite sensor, *Atmos. Chem. Phys.*,
17 14, 2555-2570, doi:10.5194/acp-14-2555-2014, 2014.

18 Wofsy, S. C.: HIAPER Pole-to-Pole Observations (HIPPO): fine-grained, global-scale
19 measurements of climatically important atmospheric gases and aerosols, *Philos. T. Roy. Soc.*
20 *A*, 369, 2073-2086, doi:10.1098/rsta.2010.0313, 2011.

21 Xiong, X., Maddy, E. S., Barnet, C., Gambacorta, A., Patra, P. K., Sun, F., and Goldberg, M.:
22 Retrieval of nitrous oxide from Atmospheric Infrared Sounder: Characterization and
23 validation, *J. Geophys. Res.-Atmos.*, 119, 9107-9122, doi:10.1002/2013JD021406, 2014.

24 Xu, X., Wang, J., Henze, D. K., Qu, W., and Kopacz, M.: Constraints on aerosol sources
25 using GEOS-Chem adjoint and MODIS radiances, and evaluation with multisensor (OMI,
26 MISR) data, *J. Geophys. Res.-Atmos.*, 118, 6396-6413, doi:10.1002/jgrd.50515, 2013.

27 Zhang, L., Jacob, D. J., Kopacz, M., Henze, D. K., Singh, K., and Jaffe, D. A.:
28 Intercontinental source attribution of ozone pollution at western US sites using an adjoint
29 method, *Geophys. Res. Lett.*, 36, L11810, doi:10.1029/2009GL037950, 2009.

1 Zhu, C., Byrd, R. H., Lu, P., and Nocedal, J.: L-BFGS-B: a limited memory FORTRAN code
 2 for solving bound constrained optimization problems, Tech. rep., Northwestern University,
 3 1994.

4 Zhu, L., Henze, D. K., Cady-Pereira, K. E., Shephard, M. W., Luo, M., Pinder, R. W., Bash, J.
 5 O., and Jeong, G. R.: Constraining U.S. ammonia emissions using TES remote sensing
 6 observations and the GEOS-Chem adjoint model, *J. Geophys. Res.-Atmos*, 118, 3355-3368,
 7 doi:10.1002/jgrd.50166, 2013.

8

9 Table 1. N₂O emissions in the a priori database and their global annual totals.

Sector	IPCC code	Global annual source (Tg N yr ⁻¹)
Agricultural soil ^a	4C+4D	3.97
Indirect emissions from agriculture ^a	4D3	0.57
Energy manufacturing transformation ^a	1A1+1A2+1B1b	0.21
Non-road transportation ^a	1A3a+c+d+e	5.0E-2
Road transportation ^a	1A3b	0.14
Oil production and refineries ^a	1B2a	4.2E-3
Industrial process and product use ^a	2	0.85
Fossil fuel fires ^a	7A	4.8E-4
Manure management ^a	4B	0.21
Residential ^a	1A4	0.18
Waste solid and waste water ^a	6	0.24
Indirect N ₂ O from NO _x and NH ₃ ^a	7B+7C	0.45
Total anthropogenic^a		6.9
Total natural soil^b		3.2
Total biomass burning^c		0.6

Total net ocean^d**3.5**

1 ^a From EDGARv4.2 for 2008

2 ^b From EDGARv2 for 1990

3 ^c From GFEDv3 (van der Werf et al., 2010)

4 ^d From Jin and Gruber (2003)

5

1 Table 2. Sites of surface flask and in situ N₂O observations used in this study

Location	Latitude	Longitude	Network ^a	Measurement type	Measurement scale
Arrival Heights, Antarctica	-77.80	166.67	NIWA	Flask	NOAA 2006A
Alert, Nunavut, Canada	82.45	-62.51	CCGG	Flask	NOAA 2006A
Argyle, Maine, USA	45.04	-68.68	CCGG	Flask	NOAA 2006A
Ascension Island	-7.97	-14.40	CCGG	Flask	NOAA 2006A
Assekrem, Algeria	23.26	5.63	CCGG	Flask	NOAA 2006A
Tereceira Island, Azores	38.77	-27.38	CCGG	Flask	NOAA 2006A
Baltic Sea, Poland	55.35	17.22	CCGG	Flask	NOAA 2006A
Boulder Atmospheric Observatory, Colorado, USA	40.05	-105.00	CCGG	Flask	NOAA 2006A
Baring Head, New Zealand	-41.41	174.87	CCGG	Flask	NOAA 2006A
Bukit Kototabang, Indonesia	-0.20	100.32	CCGG	Flask	NOAA 2006A
St. David's Head, Bermuda	32.37	-64.65	CCGG	Flask	NOAA 2006A
Tudor Hill, Bermuda	32.27	-64.88	CCGG	Flask	NOAA

					2006A
Barrow, Alaska, USA	71.32	-156.61	CCGG, CATS	Flask, in situ	NOAA 2006A
Black Sea, Constanta, Romania	44.18	28.67	CCGG	Flask	NOAA 2006A
Cold Bay, Alaska, USA	55.21	-162.72	CCGG	Flask	NOAA 2006A
Cape Ferguson, Australia	-19.28	147.05	CSIRO	Flask	NOAA 2006A
Cape Grim, Tasmania, Australia	-40.68	144.69	CCGG, AGAGE	Flask, in situ	NOAA 2006A, SIO- 98
Churchill, Manitoba, Canada	58.75	-94.07	EC	Flask	NOAA 2006
Christmas Island	1.70	-157.15	CCGG	Flask	NOAA 2006A
Cape Rama, India	15.08	73.83	CSIRO	Flask	NOAA 2006A
Crozet Island	-46.43	51.85	CCGG	Flask	NOAA 2006A
Casey Station, Antarctica	-66.28	110.53	CSIRO	Flask	NOAA 2006A
Drake Passage	-59.00	-64.69	CCGG	Flask	NOAA 2006A
Easter Island	-27.16	-109.43	CCGG	Flask	NOAA 2006A
Estevan Point, British Columbia, Canada	49.38	-126.55	EC	Flask	NOAA 2006

East Trout Lake, Saskatchewan, Canada	54.33	-104.98	EC	Flask	NOAA 2006
Fraserdale, Canada	Ontario, 49.88	-81.57	EC	Flask	NOAA 2006
Mariana Guam	Islands, 13.39	144.66	CCGG	Flask	NOAA 2006A
Gunn Point, Australia	-12.25	131.05	CSIRO	Flask	NOAA 2006A
Halley Antarctica	Station, -75.61	-26.21	CCGG	Flask	NOAA 2006A
Hohenpeissenberg, Germany	47.80	11.02	CCGG	Flask	NOAA 2006A
Hegyhátsál, Hungary	46.95	16.65	CCGG	Flask	NOAA 2006A
Stórhofdi, Vestmannaeyjar, Iceland	63.40	-20.29	CCGG	Flask	NOAA 2006A
Izaña, Canary Islands	Tenerife, 28.31	-16.50	CCGG	Flask	NOAA 2006A
Jungfrauoch, Switzerland	46.55	7.99	AGAGE	In situ	SIO-98
Key Florida, USA	Biscayne, 25.67	-80.16	CCGG	Flask	NOAA 2006A
Cape Hawaii, USA	Kumukahi, 19.52	-154.82	CCGG	Flask	NOAA 2006A
Park Wisconsin, USA	Falls, 45.95	-90.27	CCGG	Flask	NOAA 2006A

Lac La Biche, Alberta, Canada	54.95	-112.45	CCGG	Flask	NOAA 2006A
Lulin, Taiwan	23.47	120.87	CCGG	Flask	NOAA 2006A
Lampedusa, Italy	35.52	12.62	CCGG	Flask	NOAA 2006A
Mawson Station, Antarctica	-67.62	62.87	CSIRO	Flask	NOAA 2006A
Mace Head, Ireland	53.33	-9.90	CCGG, AGAGE	Flask, in situ	NOAA 2006A, SIO- 98
Sand Island, Midway Islands	28.21	-177.38	CCGG	Flask	NOAA 2006A
Mt. Kenya, Kenya	-0.06	37.30	CCGG	Flask	NOAA 2006A
Mauna Loa, Hawaii, USA	19.54	-155.58	CCGG, CATS	Flask, in situ	NOAA 2006A, NOAA 2006A
Macquarie Island, Australia	-54.48	158.97	CSIRO	Flask	NOAA 2006A
Gobabeb, Namibia	-23.58	15.03	CCGG	Flask	NOAA 2006A
Niwot Ridge, Colorado, USA	40.05	-105.55	CCGG, CATS	Flask, in situ	NOAA 2006A, NOAA 2006A
Ochsenkopf,	50.03	11.81	CCGG	Flask	NOAA

Germany						2006A
Pallas-Sammaltunturi, Finland	67.97	24.12	CCGG	Flask		NOAA 2006A
Pacific Ocean, Equator	0.00	-155.00	CCGG	Flask		NOAA 2006A
Pacific Ocean, 5 N	5.00	-151.00	CCGG	Flask		NOAA 2006A
Pacific Ocean, 10 N	10.00	-149.00	CCGG	Flask		NOAA 2006A
Pacific Ocean, 15 N	15.00	-145.00	CCGG	Flask		NOAA 2006A
Pacific Ocean, 20 N	20.00	-141.00	CCGG	Flask		NOAA 2006A
Pacific Ocean, 25 N	25.00	-139.00	CCGG	Flask		NOAA 2006A
Pacific Ocean, 30 N	30.00	-135.00	CCGG	Flask		NOAA 2006A
Pacific Ocean, 5 S	-5.00	-159.00	CCGG	Flask		NOAA 2006A
Pacific Ocean, 10 S	-10.00	-161.00	CCGG	Flask		NOAA 2006A
Pacific Ocean, 15 S	-15.00	-171.00	CCGG	Flask		NOAA 2006A
Pacific Ocean, 20 S	-20.00	-174.00	CCGG	Flask		NOAA 2006A
Pacific Ocean, 25 S	-25.00	-171.00	CCGG	Flask		NOAA 2006A

Pacific Ocean, 30 S	-30.00	-176.00	CCGG	Flask	NOAA 2006A
Pacific Ocean, 35 S	-35.00	180.00	CCGG	Flask	NOAA 2006A
Palmer Station, Antarctica	-64.92	-64.00	CCGG	Flask	NOAA 2006A
Point Arena, California, USA	38.96	-123.74	CCGG	Flask	NOAA 2006A
Ragged Point, Barbados	13.17	-59.43	CCGG, AGAGE	Flask, in situ	NOAA 2006A, SIO- 98
Beech Island, South Carolina, USA	33.41	-81.83	CCGG	Flask	NOAA 2006A
Mahe Island, Seychelles	-4.68	55.53	CCGG	Flask	NOAA 2006A
Sable Island, Nova Scotia, Canada	43.93	-60.02	EC	Flask	NOAA 2006
Southern Plains, Oklahoma, USA	Great 36.61	-97.49	CCGG	Flask	NOAA 2006A
Shemya Island, Alaska, USA	52.71	174.13	CCGG	Flask	NOAA 2006A
Tutuila, Samoa	American -14.25	-170.56	CCGG, CATS	Flask, in situ	NOAA 2006A, NOAA 2006A
South Antarctica	Pole, -89.98	-24.80	CCGG, CATS	Flask, in situ	NOAA 2006A,

					NOAA 2006A
Schauinsland, Germany	47.92	7.92	AGAGE	In situ	SIO-98
Sutro Tower, California, USA	37.76	-122.45	CCGG	Flask	NOAA 2006A
Summit, Greenland	72.60	-38.42	CCGG, CATS	Flask, in situ	NOAA 2006A, NOAA 2006A
Syowa Station, Antarctica	-69.01	39.59	CCGG	Flask	NOAA 2006A
Tae-ahn Peninsula, Korea	36.74	126.13	CCGG	Flask	NOAA 2006A
Tierra Del Fuego, Argentina	-54.85	-68.31	CCGG	Flask	NOAA 2006A
KCMP Tall Tower, Minnesota, USA	44.68	-93.07		In situ	NOAA 2006A
Trinidad Head, California, USA	41.05	-124.15	CCGG, AGAGE	Flask, in situ	NOAA 2006A, SIO- 98
Wendover, USA	Utah, 39.90	-113.72	CCGG	Flask	NOAA 2006A
Ulaan Uul, Mongolia	44.45	111.10	CCGG	Flask	NOAA 2006A
West Branch, USA	Iowa, 41.73	-91.35	CCGG	Flask	NOAA 2006A
Walnut Grove, USA	38.27	-121.49	CCGG	Flask	NOAA

California, USA						2006A
WIS Station, Negev, Israel	30.86	34.78	CCGG	Flask	NOAA	2006A
Moody, Texas, USA	31.32	-97.33	CCGG	Flask	NOAA	2006A
Mt. Waliguan, China	36.29	100.90	CCGG	Flask	NOAA	2006A
Western Pacific Cruise	-30.00 to 30.00	136.80 to 168.00	CCGG	Flask	NOAA	2006A
Ny-Ålesund, Svalbard, Norway	78.91	11.89	CCGG	Flask	NOAA	2006A

- 1 ^a CCGG: NOAA Carbon Cycle and Greenhouse Gases program; EC: Environment Canada;
- 2 NIWA: National Institute of Water and Atmospheric research; CATS: NOAA Chromatograph
- 3 for Atmospheric Trace Species; AGAGE: Advanced Global Atmospheric Gases Experiment.

1 Table 3. Global annual N₂O a posteriori source for all pseudo observation tests

Observations	State vector	Initial bias	A posteriori flux (Tg N yr ⁻¹) ^a	A posteriori sink (Tg N yr ⁻¹) ^b
Surface	Emissions	0.5, 1.5	14.16, 14.25	--
CARIBIC	Emissions	0.5, 1.5	13.82, 14.72	--
HIPPO	Emissions	0.5, 1.5	14.12, 14.27	--
Surface	Emissions + Strat loss frequencies	0.5, 1.5	14.04, 14.84	7.73, 24.91
CARIBIC	Emissions + Strat loss frequencies	0.5, 1.5	13.63, 15.40	6.13, 19.72
HIPPO	Emissions + Strat loss frequencies	0.5, 1.5	14.00, 14.74	7.65, 22.60
Surface	Strat loss frequencies	0.5, 1.5		12.02, 12.93
CARIBIC	Strat loss frequencies	0.5, 1.5		10.09, 14.66
HIPPO	Strat loss frequencies	0.5, 1.5		10.60, 13.99
CARIBIC (no transport error)	Emissions + strat loss frequencies	0.5	14.16	9.94
HIPPO (no transport error)	Emissions + strat loss frequencies	0.5	14.14	11.39
CARIBIC (no transport error)	Strat loss frequencies	0.5		11.57
HIPPO (no transport error)	Strat loss frequencies	0.5		12.03
Surface	Emissions	Seasonal	13.63	

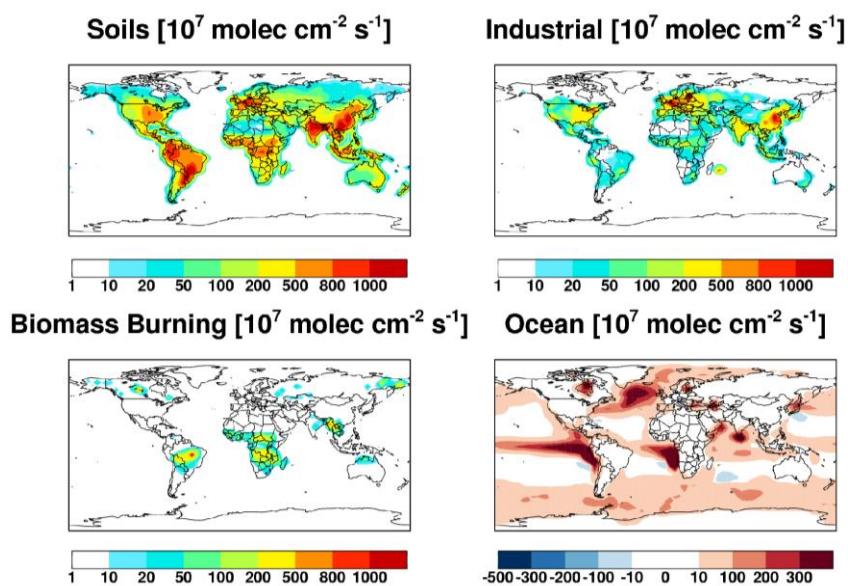
CARIBIC	Emissions	Seasonal	13.59
HIPPO	Emissions	Seasonal	13.44

1 ^a True model flux is 14.16 Tg N yr⁻¹

2 ^b True model stratospheric sink is 12.1 Tg N yr⁻¹

3

4

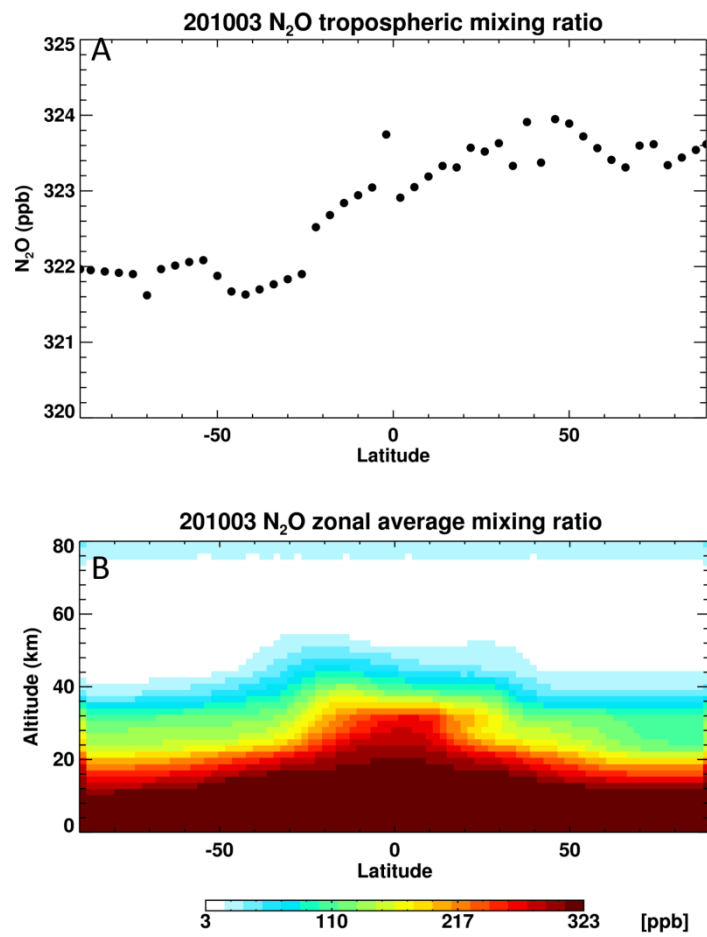


5

6 Figure 1. Mean annual N₂O fluxes from soils, industrial activities, biomass burning, and ocean
7 exchange in the GEOS-Chem a priori simulation.

8

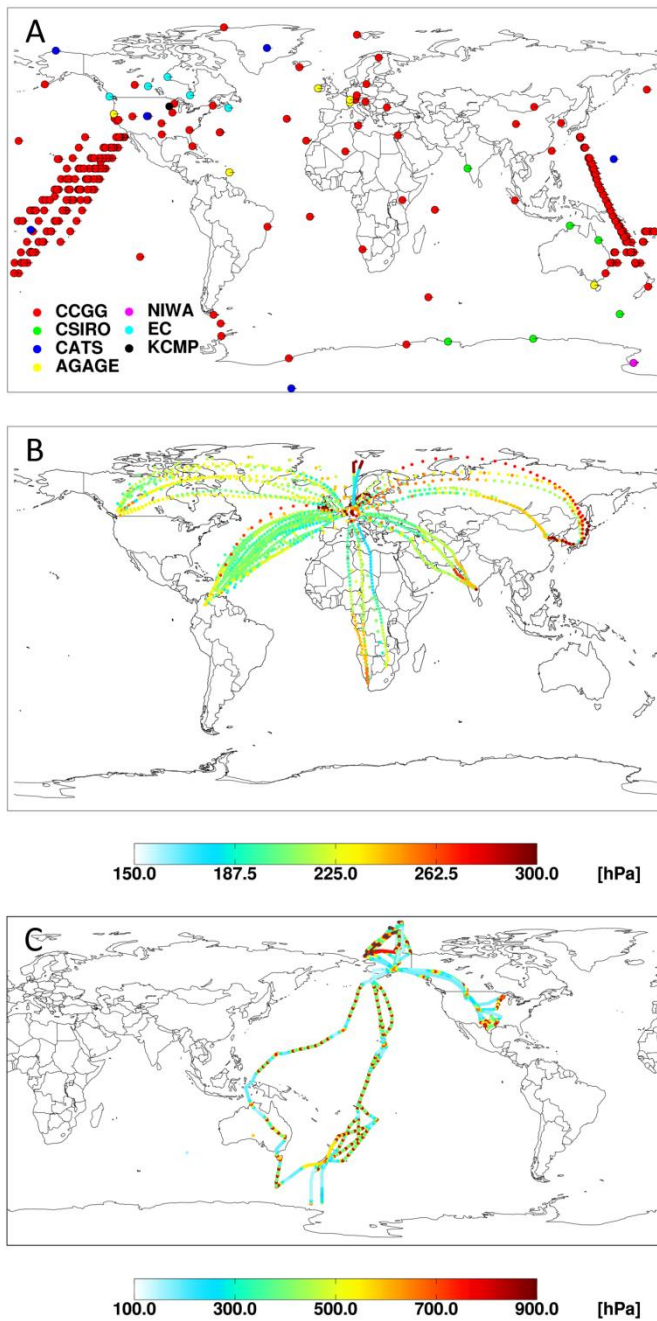
9



1
2 Figure 2. Initial model N_2O field for March 2010. Shown are the (A) tropospheric N_2O mixing
3 ratios, and (B) zonal mixing ratio cross-section.

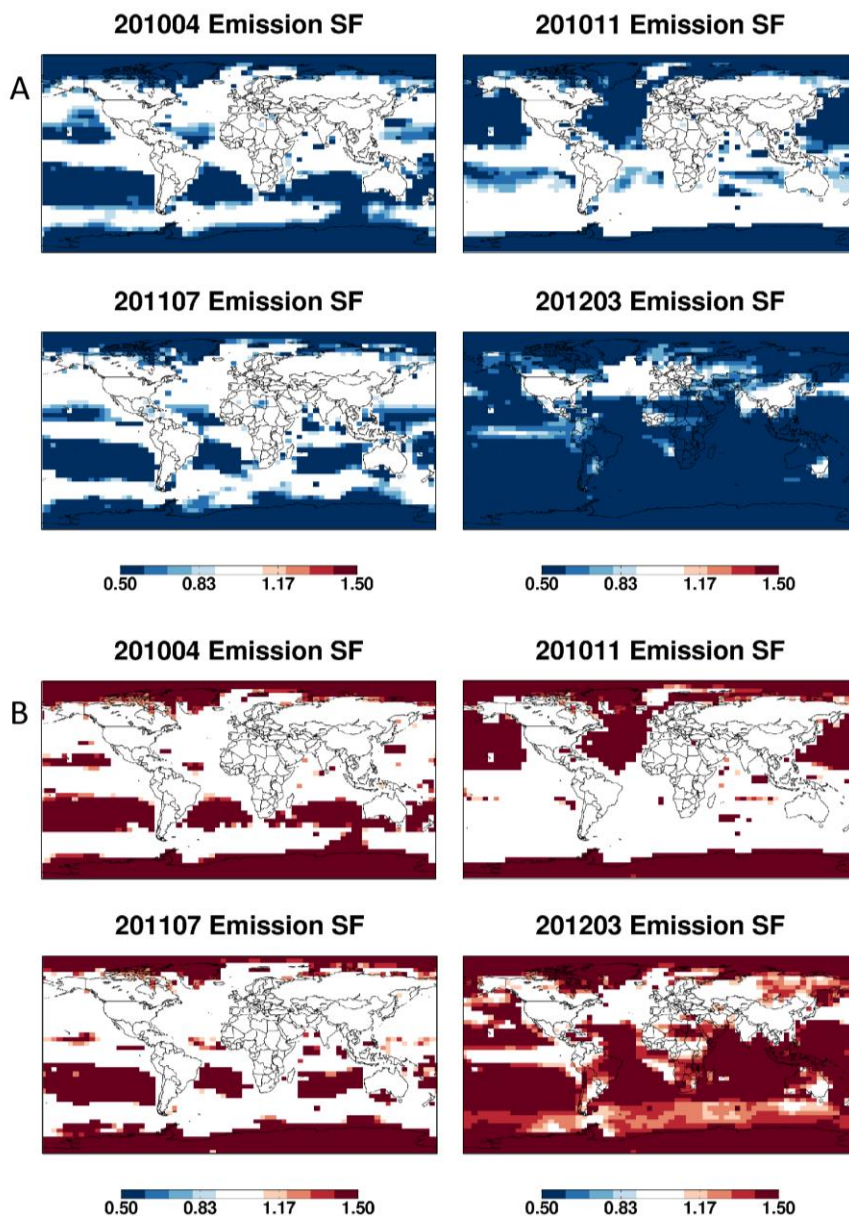
4

5



1
 2 Figure 3. Global observing network for atmospheric N_2O . Shown are the locations of (A)
 3 surface observations, (B) CARIBIC aircraft observations, and (C) HIPPO aircraft
 4 observations. The CARIBIC and HIPPO flights are shaded by the pressure at which the
 5 observations were made. Color scales differ between panels (B) and (C) to show the range of
 6 vertical sampling in each case.

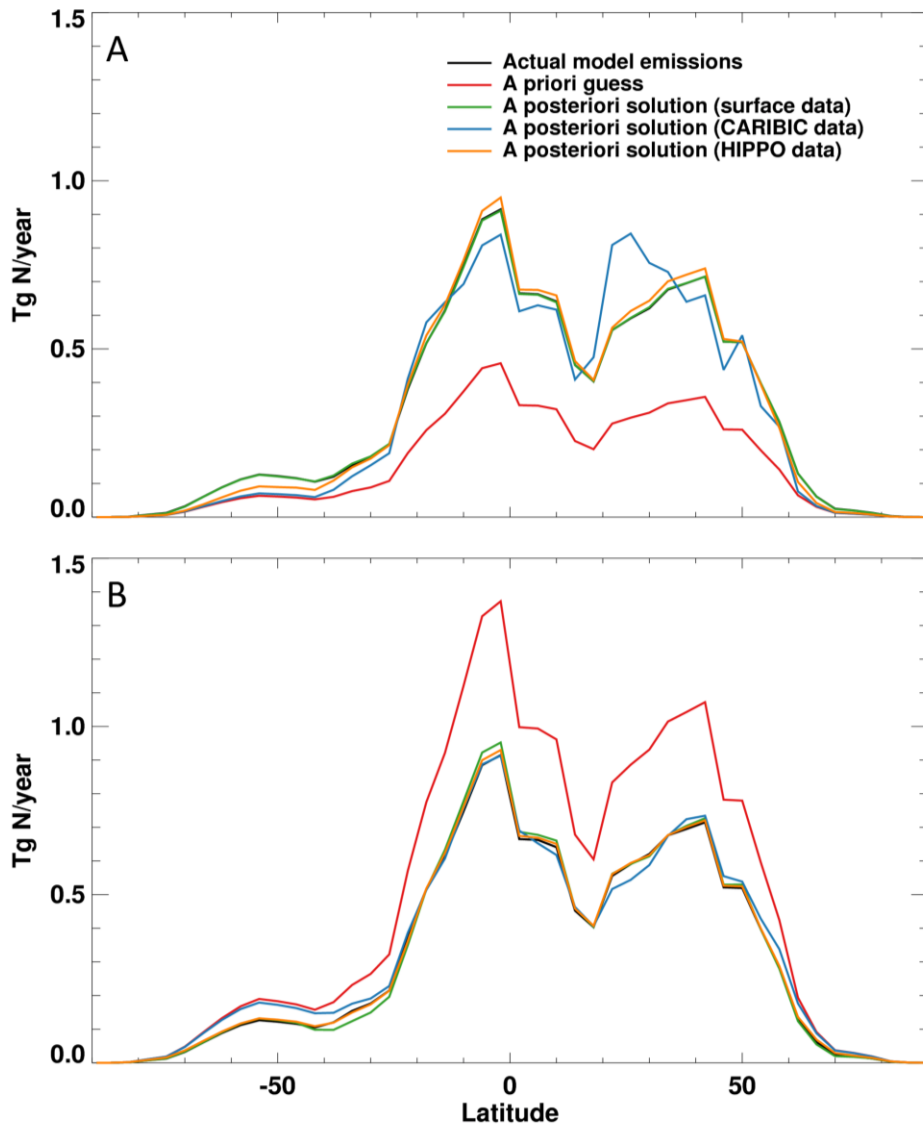
7



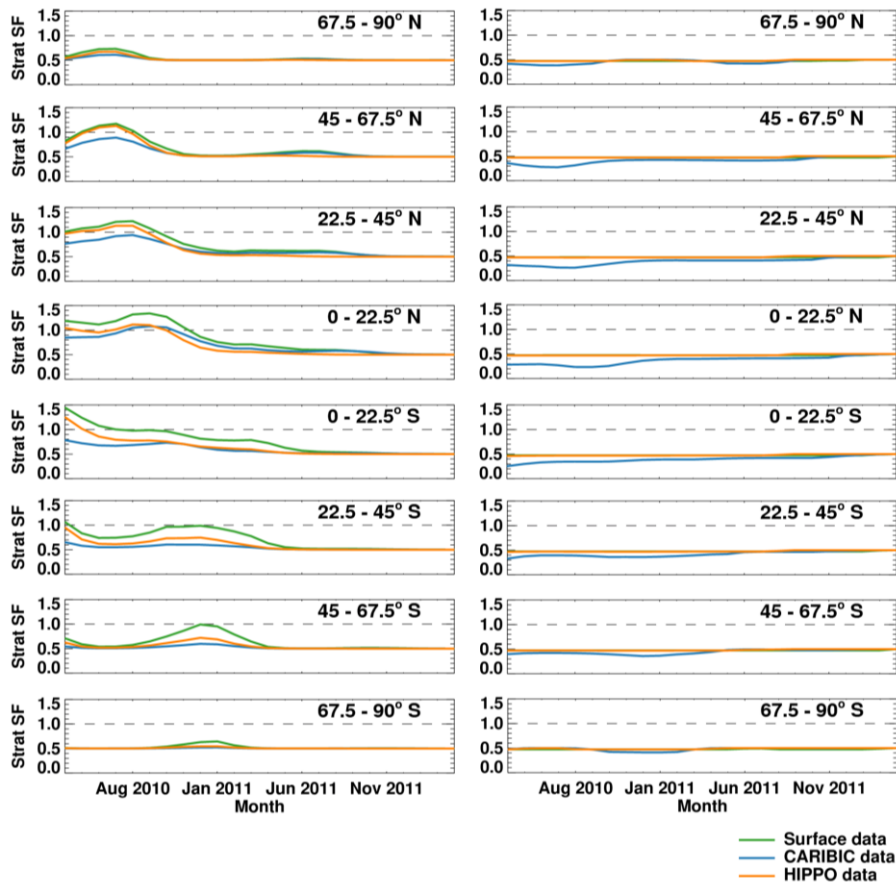
1
 2 Figure 4. Pseudo observation test optimizing N₂O emissions on the basis of surface
 3 observations. Shown are a posteriori emission scaling factors using an a priori guess of either
 4 (A) 0.5 or (B) 1.5, where the true value is 1.0. Results are shown for April 2010 (month 1 of
 5 the inversion window), November 2010 (month 8), July 2011 (month 16), and March 2012
 6 (month 24).

7

8



1
 2 Figure 5. Pseudo observation tests optimizing N₂O emissions. Shown are zonally-integrated
 3 annual emissions for the first year of the simulation (April 2010 – March 2011) starting with
 4 an a priori scaling factor of (A) 0.5 and (B) 1.5, where the true value is 1.0. Actual model
 5 emissions are shown in black, model emissions scaled by the a priori guess are shown in red,
 6 and a posteriori emissions obtained using surface data, CARIBIC data, and HIPPO data are
 7 shown in green, blue, and yellow, respectively.

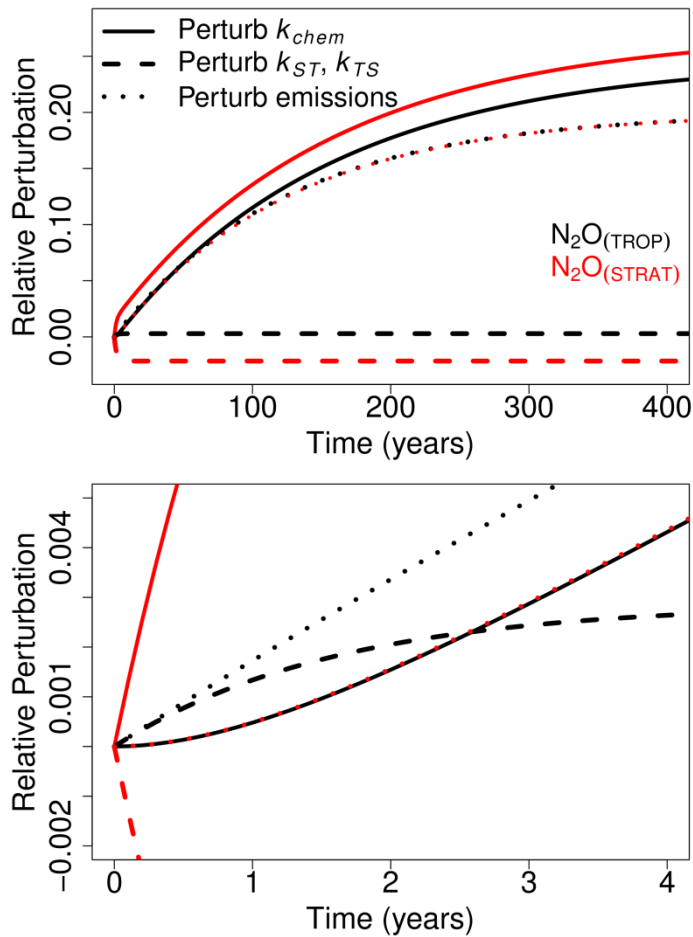


1

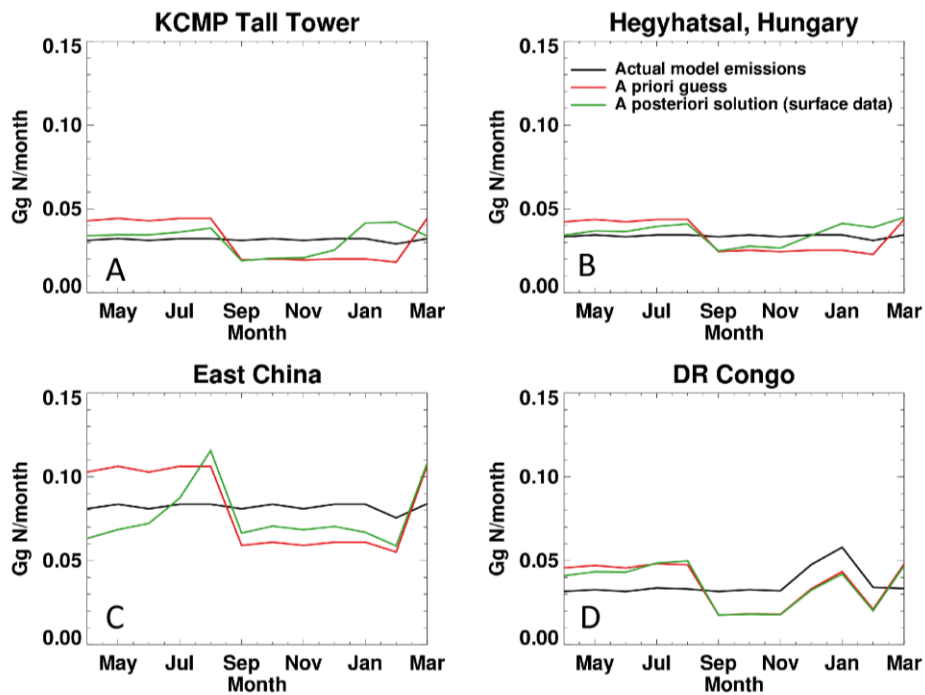
2 Figure 6. Pseudo observation tests optimizing N_2O stratospheric loss frequencies. Shown are a
 3 posteriori scaling factors (SF) for stratospheric loss frequencies in each of eight equal latitude
 4 bands for pseudo observation tests in which we optimize solely the stratospheric loss
 5 frequencies (left panels) or the emissions and stratospheric loss frequencies jointly (right
 6 panels). The latitude range of each band is indicated in the upper right hand corner of each
 7 panel. The true model value (1.0) is indicated by the black dashed line; each test started with a
 8 priori SF of 0.5 for each latitude band. Results obtained using surface data, CARIBIC data,
 9 and HIPPO data are shown in green, blue, and yellow, respectively.

10

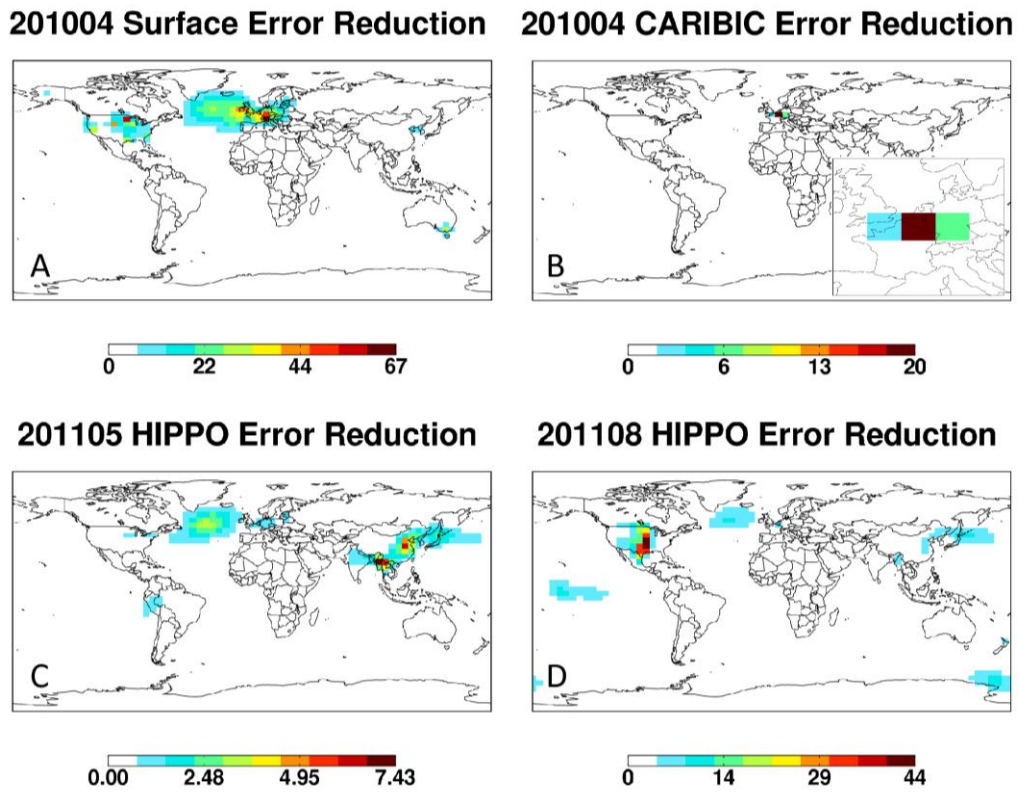
11



1
 2 Figure 7. Results from a 2-box model illustrating the sensitivity of the tropospheric N_2O
 3 burden (and hence source inversions) to the N_2O stratospheric loss rate and to the rate of
 4 stratosphere-troposphere exchange. Shown are the relative perturbations to the tropospheric
 5 (black lines) and stratospheric (red lines) N_2O burdens resulting from: a 20% change in the
 6 N_2O stratospheric loss frequency (Perturb k_{chem} , solid lines); a 20% change in the rate of
 7 stratosphere-troposphere exchange (Perturb k_{ST}, k_{TS} , dashed lines); and a 20% change in
 8 emissions (Perturb emissions, dotted lines). The top panel shows results over a 400-year
 9 timescale, while the bottom panel shows the initial 4 years.

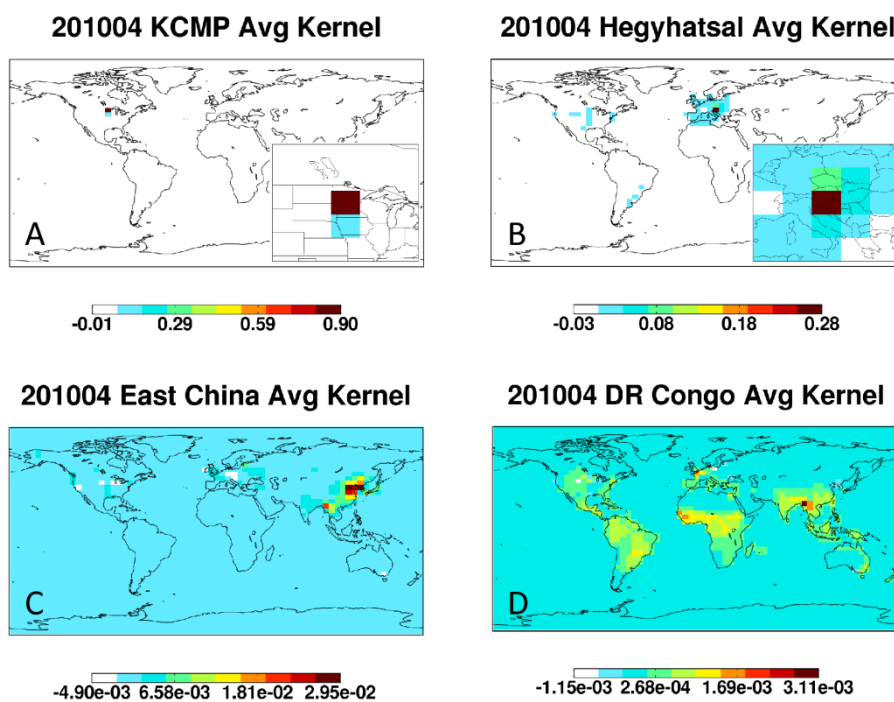


1
 2 Figure 8. Resolving seasonal emission biases. The panels show the results from an OSSE in
 3 which a seasonally-dependent a priori emission bias is applied and we test the ability of the
 4 inversion to recover the true model fluxes. Results are shown for a site with continuous
 5 observations (KCMP Tall Tower), a site with ~weekly flask observations (Hegyhátsál,
 6 Hungary), a site with routine flask measurements ~1000 km downwind (East China), and a
 7 remote site in the Democratic Republic of Congo (DR Congo). The a priori (red), a posteriori
 8 (green) and true model fluxes (black) are plotted for the first year of the simulation (April
 9 2010 – March 2011), with the a priori guess for soil emissions biased high in the first half of
 10 the inversion period (1.5×; March – August) and biased low in the second half (0.5×;
 11 September – February).
 12



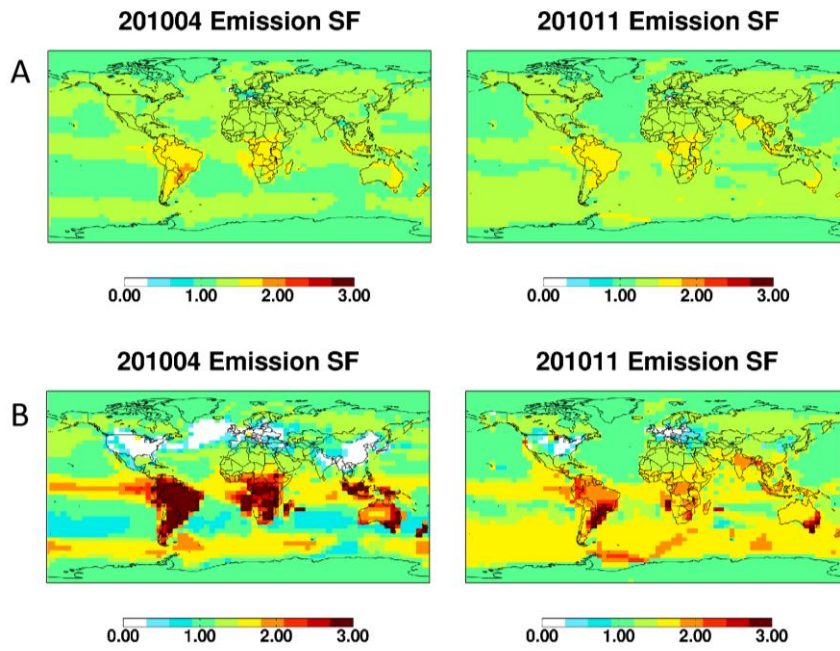
1
 2 Figure 9. Error reduction (%) in N₂O emissions achievable in selected months using surface
 3 (A), CARIBIC (B), and HIPPO (C and D) measurements. An inset shows regional detail for
 4 the CARIBIC results. The relative error reduction is calculated based on a stochastic estimate
 5 of the inverse Hessian of the cost function for the inversion, and represents the ability of the
 6 observing system to remove a random emission error for each given location in the absence of
 7 any large-scale source bias.

8

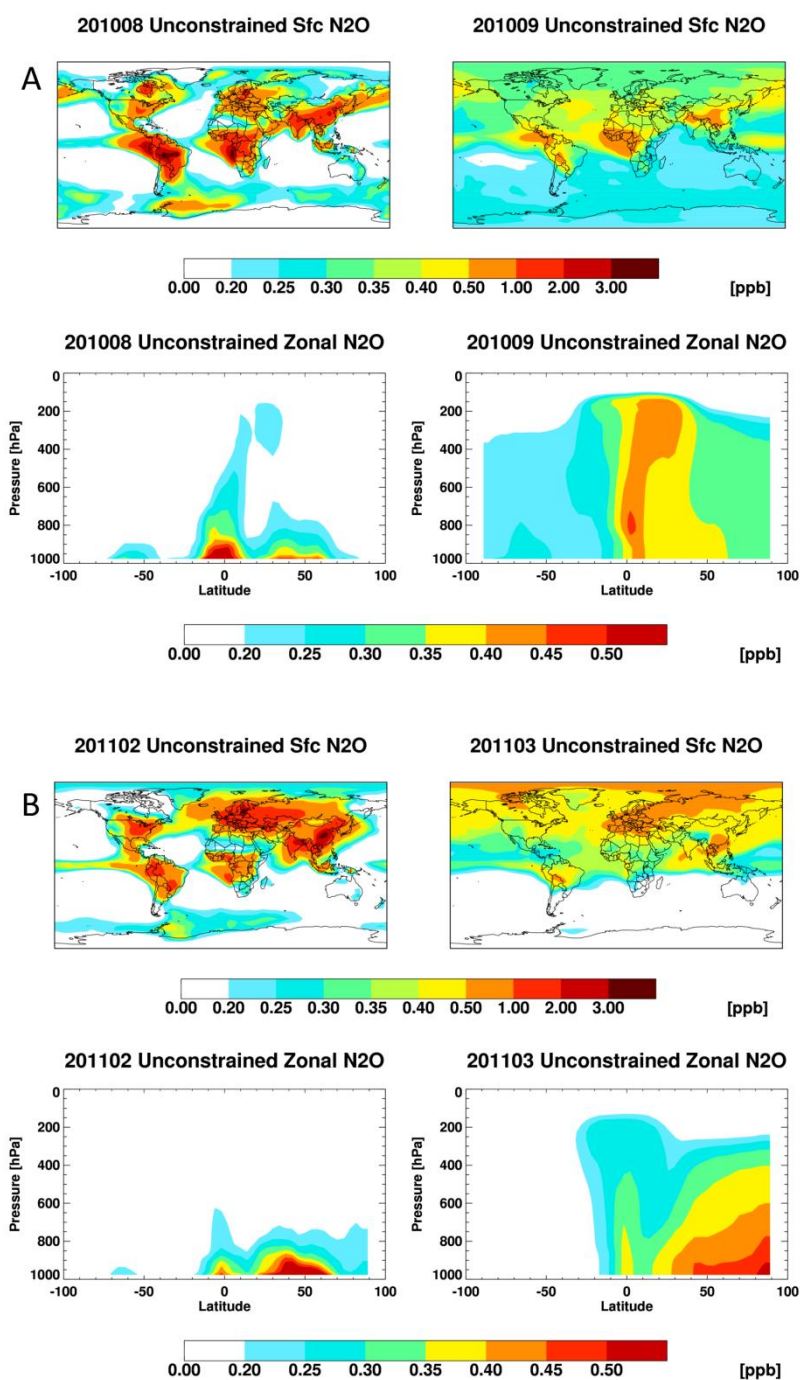


1
 2 Figure 10. Rows of the averaging kernel for the inversion of N₂O emissions based on surface
 3 observations. The results indicate how well emissions in a particular location can be resolved
 4 from emissions elsewhere, and are shown for four example sites: (A) KCMP tall tower, (B)
 5 Hegyhátsál, Hungary, (C) a grid cell in East China, and (D) a grid cell in the Democratic
 6 Republic of Congo. Insets show regional detail for the first two sites. KCMP is a site with
 7 continuous observations, Hegyhátsál is a site with ~weekly flask observations, the East China
 8 site is a location with flask observations ~1000 km downwind, and the Congo site is a remote
 9 location.

10
 11
 12



1
 2 Figure 11. Inversion of N_2O emissions based on real surface observations. A posteriori
 3 emission scaling factors are shown for two different prior error assumptions: (A) 100% a
 4 priori error and horizontal covariance length scales of 500 and 1000 km for land and ocean
 5 emissions, respectively; and (B) no penalty term in the cost function.



1
 2 Figure 12. Distribution of unconstrained N₂O simulated by GEOS-Chem during the month of
 3 emission (August 2010 and February 2011) and the subsequent month. Unconstrained
 4 concentrations are calculated by scaling emissions for a particular month by $(1 - x)$, where x
 5 is the map of emission error reductions achieved using surface observations of N₂O. The initial
 6 atmospheric burden of N₂O and the emissions in the ensuing months are set to zero in order to
 7 highlight the spatial dispersal of unconstrained N₂O. Note nonlinear color scales.